nature physics

Article

https://doi.org/10.1038/s41567-026-03305-4

The physical consequences of sperm gigantism

Received: 9 August 2025

Accepted: 20 April 2026

Published online: 22 June 2026

Check for updates

Jasmin Imran Alsous[1,5], Brato Chakrabarti[2,5], Bryce Palmer[1,3] & Michael J. Shelley[1,4]

Males of the fruit fly *Drosophila melanogaster* produce sperm that are each, on average, a couple of millimetres long. Thousands of sperm are stored in a seminal vesicle of only about 200 µm in size. Although the evolutionary pressures underlying such extreme flagellar lengths have been investigated, the physical consequences of their gigantism remain unclear. Here we show that sperm are packed into a dense and highly aligned state. We also find that sperm exhibit system-wide collective material flows with persistent and slow-moving topological defects. Individual sperm, despite their extraordinary lengths and in contrast to their feeble motility in isolation, propagate rapidly through the flagellar material, moving in either direction along material director lines. To rationalize how these collective behaviours arise from the non-equilibrium dynamics of the constituents, we conceptualize the motion of individual sperm as topologically confined to a reptation-like tube formed by its neighbours. Here sperm advance through amplitude-constrained and internally driven bending waves, pushing off counterpropagating flagella. We derive a continuum theory that produces an extensile stress that can sustain an aligned flagellar material, and verify theoretical predictions. Our work suggests that active stresses in the flagellar material maintain the sperm unentangled in both male and female storage organs and establishes giant sperm in their native habitat as a physiologically relevant active matter system.

Some animals produce exceptionally long sperm, comparable with the animal itself, and exceeding the distance travelled in the female. Such 'giant' sperm have evolved in several animal taxa[1–7] for >100 million years[8]—a testament to the enduring success of sperm gigantism as a sexual strategy. Males of the fruit fly *Drosophila melanogaster*—a powerful and relevant organism for the quantitative and mechanistic studies of reproduction and post-copulatory sexual selection[9–16], produce ~1,800-µm sperm (Fig. 1a and Extended Data Fig. 1)[17,18]. Most of the sperm's length is accounted for by a relatively thick ($d \approx 0.5$–0.7 µm (refs. 19,20)) and active flagellum (tail) that is powered by bending waves generated by the conserved microtubule-based axoneme (Supplementary Video 1)[21–24]; the needle-shaped head is merely ~10 µm long. Sperm produced in the testes as bundles are deposited as individuals in two seminal vesicles (SVs), which are $L \approx 200$ µm teardrop-shaped sacs that can store thousands of such ultralong sperm until mating[25–27] (Fig. 1b,c and Supplementary Fig. 1). The dense packing of long, slender objects is a ubiquitous biological phenomenon—perhaps its most notable biological realization being the packing of metres of chromosomal DNA within a 10-µm human nucleus[28]. An important class of these problems arises when the filaments themselves are internally active; one such example is the centimetric California blackworm, hundreds of which can form a tightly wound three-dimensional (3D) tangled structure, but can

[1]Center for Computational Biology, Flatiron Institute, New York, NY, USA. [2]International Centre for Theoretical Sciences, Tata Institute of Fundamental Research, Bengaluru, India. [3]Department of Mechanical Engineering, Michigan State University, East Lansing, MI, USA. [4]Courant Institute, New York University, New York, NY, USA. [5]These authors contributed equally: Jasmin Imran Alsous, Brato Chakrabarti. e-mail: mshelley@flatironinstitute.org

https://doi.org/10.1038/s41567-026-03305-4

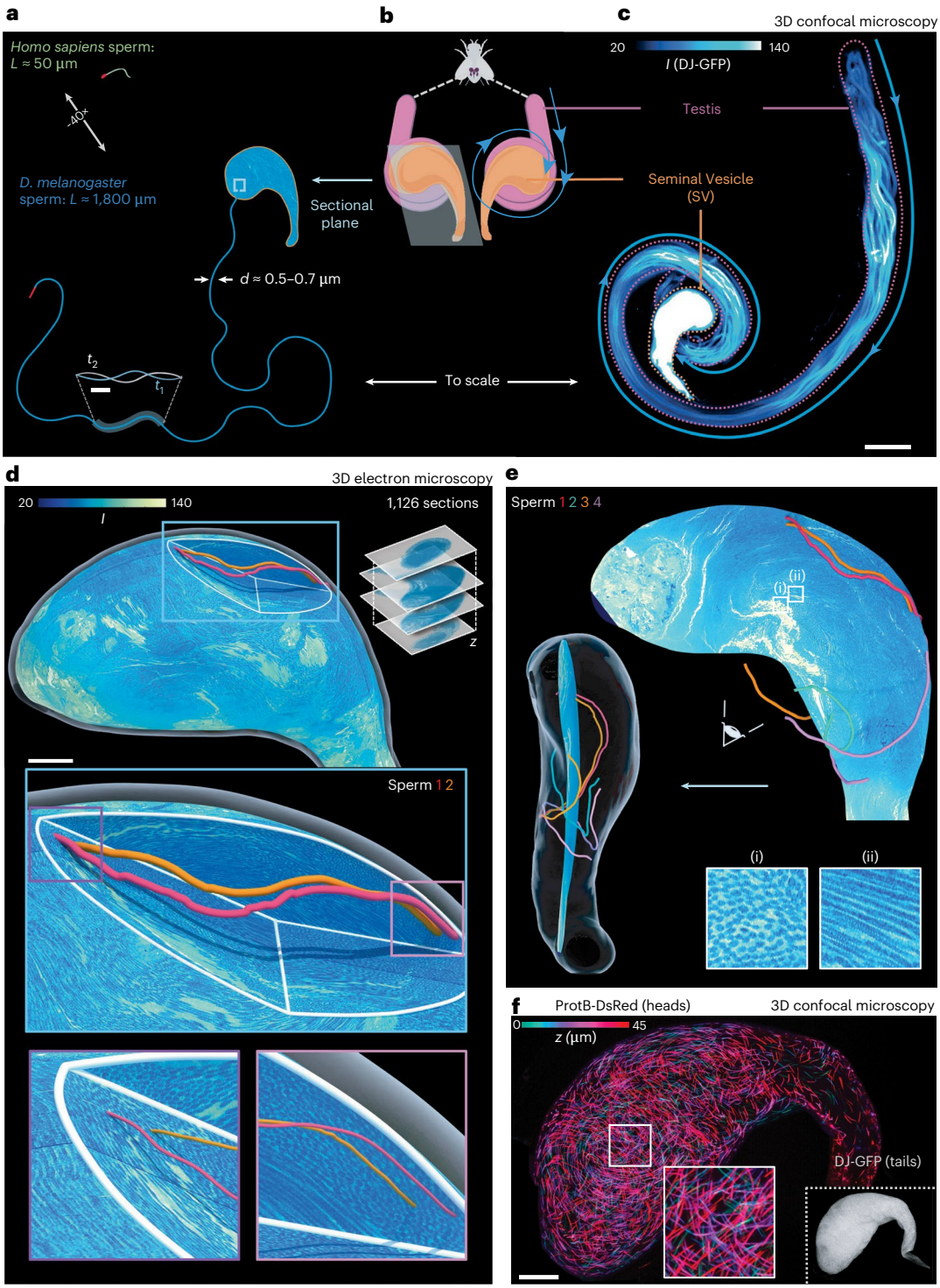

Fig. 1 | 3D organization and packing of giant *D. melanogaster* sperm in the SV. a, Schematic of a single *D. melanogaster* sperm traced from a confocal image (Extended Data Fig. 1) shown to scale relative to a *Homo sapiens* sperm and to the male's sperm storage organ, the SV, in **b** and **c**. The sperm generates bending waves (Supplementary Video 1); the inset shows two overlaid successive time points. Scale bar, 10 µm. **b**, Simplified schematic of the male's reproductive system. Sperm produced in the ~2-mm-long testes (magenta) are deposited in a pair of SVs (orange). **c**, Maximum intensity projection (MIP) of fluorescently labelled sperm flagella in the testis and mature sperm in the SV. Colour encodes the DJ-GFP signal intensity, highlighting the dense packing of sperm in the SV. Scale bar, 100 µm. **d**, A 3D rendered image of all sperm in the SV, coloured by intensity *I*, acquired through SBF-SEM of the entire storage organ, with a voxel size of 10 nm in the *x*–*y* direction and 100 nm along the *z* direction (Extended Data Fig. 2 and Supplementary Video 2). A portion of the data is digitally removed to expose the packing of sperm in the bulk; partial views of two segmented sperm (orange and magenta), spanning regions of distinct local alignment, are shown. Scale bar, 20 µm. **e**, A single SBF-SEM section with four partially segmented sperm. A different viewing angle, with the SV's boundary demarcated (white shell), is also shown. Two regions (white boxes) are magnified to highlight the individual sperm's out-of-plane (i) and in-plane (ii) arrangement. **f**, MIP of fluorescently labelled sperm heads (ProtB-DsRed), colour coded by depth (*z*) in the SV (Supplementary Video 2), with one region magnified. Scale bar, 20 µm. The rightmost inset is the corresponding MIP of the flagella (DJ-GFP).

rapidly disentangle under duress[29]. Ultralong sperm must resist knots and tangles to travel within and across reproductive tracts[30,31], raising questions about how these cells organize[2], and how their autonomous activity and interactions manifest within these tight confines.

Here we report the discovery of an in vivo active matter system in which dense collectives of giant sperm organize into an aligned and structured motile state, punctured only by spontaneous and persistent topological defects, resembling a living liquid crystal[32,33]. Highly resolved and rapid microscopy, perturbation experiments and simulations of active elastic filaments demonstrate that these dynamics arise from contact interactions between counterpropagating sperm that actively reptate within the flagellar mass. A minimal and experimentally constrained coarse-grained theory built on this conception rationalizes the sperm's ordered motility, separation of timescales and system-wide flagellar flows in the SV, as well as the sperm's dynamics in the female's primary storage organ. Our work suggests a role for active material stresses in fluidizing sperm in their native microenvironment, with implications for the animal's fertility.

3D in vivo organization of giant sperm

We first set out to reconstruct the sperm's 3D organization and packing in the SV, readily extractable from the abdomen through dissection (Fig. 1a,b and Supplementary Section I.B). Using serial block-face scanning electron microscopy (SBF-SEM), we acquired a volumetric image of the SV and its resident sperm. By revealing the nanoscale ultrastructure and anatomical features[34], SBF-SEM allows us to resolve all individual sperm in the entire organ (Supplementary Video 2 and Supplementary Section I.C). We discovered that the SV (~200 μm × 150 μm × 150 μm), independent of the sectional orientation (Extended Data Fig. 2), is densely packed with sperm whose alignment is correlated over a length scale of ~48 ± 12 μm ($n = 8$ +1/2 defect pairs from five SVs; Supplementary Section II.D). 3D reconstructed segmentations reveal that a sperm meanders through the SV, with periodic, low-amplitude undulations along its flagellar backbone, presumably resulting from internally generated deformation waves (Fig. 1d, middle). The sperm's length, longer than the correlation length of the director orientation, suggests that its flagella transits through multiple regions of varying nematic orientation (Fig. 1e).

We also performed 3D confocal imaging of sperm whose flagella and heads were illuminated through the fluorescent labelling of Don Juan protein (DJ-GFP), a male germline-specific mitochondrial protein found along the entire length of the ~1,800-μm flagellum[35], and protamine B (ProtB-DsRed), a protein involved in DNA compaction[36], respectively (Supplementary Section I.B). Consistent with our SBF-SEM data, we found that sperm in the SV are packed into a dense, aligned state—evident from examining the spatial organization of both their relatively short heads and much longer flagella (Fig. 1f). We estimate the sperm's volume fraction φ in the SV ranges from ~40%–60% (Supplementary Section II.H).

Collective material flows and individual laning

We next turn to the sperm's dynamics. Supplementary Video 3 shows a time lapse that captures the individual and collective motion of sperm in their dense in vivo environment, visible through the fluorescent labelling of the sperm's heads and flagella, respectively. These data reveal that in contrast to the passive, bundled and immotile sperm in the testes (Fig. 1c)[25,37], sperm in the SV are highly motile. Specifically, the sperm's flagella fold and bend collectively, resulting in continuously evolving and coherent, system-wide flagellar material flows, lasting for hours following SV extraction (Fig. 2 and Supplementary Video 3). We also observe persistent ±1/2-order topological defects (Fig. 2a–c), whose cores are devoid of sperm, spontaneously formed by the folding of long flagella, similar to the defects formed by deforming fibres in cavities[38] and growing long-chain bacterial colonies[39]. In a nematic field, such ±1/2 defects are singular points around which the director's local orientation rotates by 180°: the +1/2 defect has a comet-like, polar shape and is motile, whereas the −1/2 defect has a three-fold symmetric structure and is largely stationary[40]. Gradients in the director field near these defects drive material stresses and local flows; however, unlike in other active nematics such as epithelial monolayers[41], where anisotropic friction leads to density accumulation near +1/2 defects[42,43], sperm in the SV appear to maintain nearly uniform density away from the defects' voids. Live imaging further reveals that flagella are highly aligned, as characterized by the scalar order parameter S, obtained from the local nematic tensor constructed from tangent vectors along the sperm's centre lines (each filament is represented as a series of short rod-like segments, whose tangent orientations are locally averaged; Supplementary Section II.A). The nematic director field shows that changes in flagellar orientation occur over a characteristic length scale $L_d \approx 70 \pm 11$ μm, given by the separation distance of pairs of +1/2-order defects (Fig. 2e), in agreement with the correlation length measured from fixed SVs.

By tracking the moving comet-shaped +1/2-order topological defects, we obtained a proxy value for the material speed as $U \approx 2.4 \pm 0.9$ μm s^{-1}; −1/2-order defects are, by contrast, much slower, moving at ~0.68 ± 0.24 μm s^{-1} (Fig. 2g and Supplementary Section II.C). The direction of motion of the +1/2-order defects (rear to front) indicates that the flagellar material is under extensile (← →), rather than contractile (→ ←), stress along the material director field[41]. The orientation of the director field changes with a characteristic timescale of $\tau \approx 45 \pm 15$ s (Fig. 2f)—interpretable as a measure of the inverse time associated with the mean vorticity of the material flow (Supplementary Section II.D). Given a system size $L \approx 200$ μm, we find that $U \approx L/\tau \approx 3$–4 μm s^{-1}—in agreement with the measurements of +1/2-order defect speeds.

From the same microscopy data, we also tracked the sperm's needle-shaped heads: being the same width as the flagellum, yet much shorter, the ~10-μm-long heads serve as natural, sparser markers for sperm motion through the dense flagellar material (Fig. 1a and Extended Data Fig. 1). We found that sperm swim past each other along the nematic director lines, and do so relatively quickly ($v_s \approx 15.6 \pm 5.1$ μm s^{-1}) compared with the material speed U (Fig. 2g). When successive frames in a time lapse are superimposed, the sperm's laning dynamics can be captured in a still (Fig. 2d), just as long-exposure photography captures the laning of cars on highways.

We also acquired time lapses of fluorescently labelled sperm in SVs that have been compressed under a coverslip (Supplementary Section I.B). In such a setup, the sperm's out-of-plane motion is suppressed, thereby confining the dynamics to a quasi-two-dimensional (2D) geometry, and sperm experience enhanced friction with the confining tissue. Nonetheless, we observe system-wide material flows with qualitatively similar features as those observed in the uncompressed SV (Fig. 5a,b, Extended Data Fig. 4 and Supplementary Video 5), suggesting that out-of-plane flagellar motion is not central to the emergent material flows.

In contrast to the persistent and directional motility of the sperm in the SV (Fig. 2a and Supplementary Video 3), sperm released from the SV into the surrounding buffer remain largely stationary, despite waves of deformation moving along their flagella (Supplementary Video 1). The weak or absent progressive motility of isolated *Drosophila* sperm in vitro[22,44,45] and of giant sperm in other species[24,46] contrasts with that of self-propelled cells, such as mammalian sperm or bacteria. These data suggest that the spatial restriction of the in vivo environment underpins sperm's directed motility.

Photomanipulation reveals apolar organization

As a first step towards understanding the mechanism and nature of interactions that underlie the sperm's individual dynamics and emergent material flows, we characterized the sperm's relative motion in vivo. Again using time lapses of sperm in the SV, we identified and examined over 1,100 contiguous pairs of fluorescently labelled heads

https://doi.org/10.1038/s41567-026-03305-4

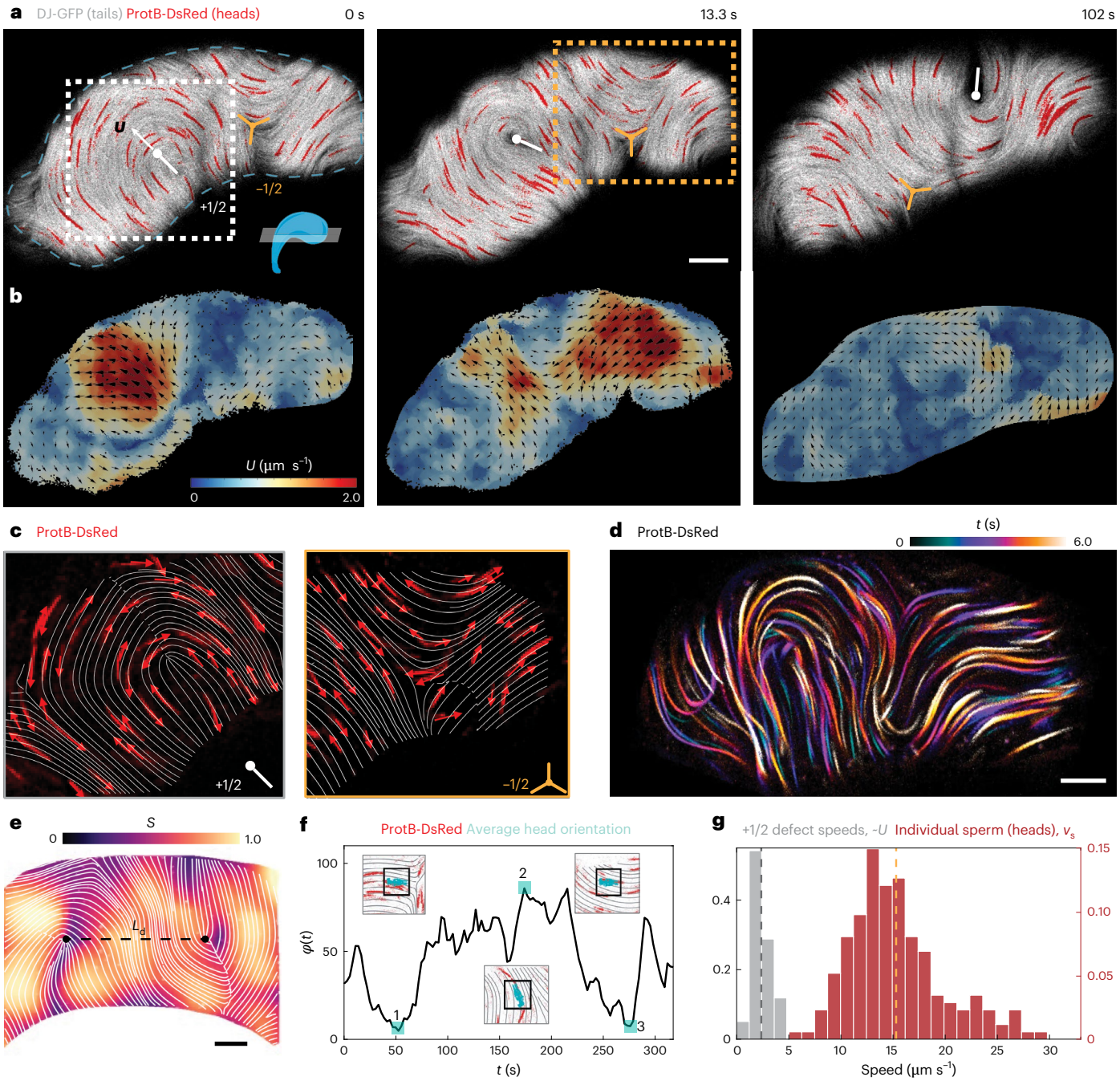

Fig. 2 | Spatiotemporal dynamics of individual giant sperm and their collective flows in vivo. a, Snapshots from a time lapse of fluorescently labelled sperm (tails or flagella in grey; heads in red) in an optical section through the SV, ~20 μm from the organ's surface (blue dashes at $t = 0$ s delineate the SV's boundary). The flagella exhibit continuously evolving system-wide 'material' flows, characterized by alignment and persistent ±1/2-order topological defect dynamics (Supplementary Video 2). Magnified views of the boxed regions are shown in **c**. **b**, Material velocity fields with the magnitude of U (colour coded); arrows are velocity vectors. The measurement of $U \approx 2$ μm s^{-1} through the optic flow is in agreement with the estimate obtained by measuring the timescale of evolution of the local average director orientation (see **f**) and from tracking the motion of +1/2-order defects (see **g**). **c**, Sperm heads (ProtB-DsRed, red) with an overlaid nematic director field in proximity to a +1/2-order (left) and a −1/2-order (right) defect. Sperm swim along the nematic director field lines (arrows indicate their direction of motion) more rapidly ($v_s \approx 15$ μm s^{-1}) than the emergent flagellar material flows (see **g**). **d**, Colour-coded MIP of successive frames from a 6-s window from the time lapse of an SV with fluorescently labelled heads (ProtB-DsRed), capturing the sperm's laning behaviour. **e**, Snapshot of an SV from the time lapse with an overlaid nematic director field (white), showing the separation between a pair of +1/2-order defects (average $L_d \approx 70 \pm 11$ μm, $n = 12$ +1/2-order defect pairs). The nematic order parameter $0 \le S \le 1$ is colour coded. Scale bars, 10 μm (**a**, **d** and **e**). **f**, Average orientation of sperm heads (ProtB-DsRed, red) in a region of interest (ROI; black) in an optical slice over time, from which we estimate the characteristic timescale of reorientation of the flagellar material τ ($n = 13$). Insets show the heads' average orientation (cyan) within that ROI, with the overlaid director field (black). **g**, Histograms of the speeds of individual sperm (red) and +1/2-order defect (grey), highlighting a separation of timescales; the dashed lines indicate the respective averages ($n = 174$ individual sperm in 9 SVs; $n = 59$ +1/2-order defects in 11 SVs; −1/2-order defects are much slower, with speeds of ~0.68 ± 0.24 μm s^{-1}, $n = 10$ +1/2-order defects in 4 SVs).

(separated by less than ~0.5 μm) at various depths and locations, and found that in ~79% of cases, sperm swam in opposite directions (Fig. 3a,b and Supplementary Section II.F). To relate these data to the behaviour of the flagella, we selectively photobleached fluorescently labelled flagella in different regions of the SV, thereby marking a subset of flagellar segments. This experiment uncovers the relative dynamics of individual tails in the dense assembly—an approach effectively used in active in vitro motor-driven microtubule assemblies[32,47]. We confirmed that the director field intensity and individual sperm speeds remained largely unaltered pre- and post-photobleaching (Supplementary Section II.G).

Our data reveal that adjacent photobleached flagellar segments move predominantly in opposite directions along the field lines (Fig. 3c–f and Supplementary Video 4), consistent with results obtained from tracking head pairs. The extent of the sperm's interdigitation can be measured by Λ, defined as the distance between two bleached segments moving in the same direction, separated by one or more bleached segments moving in the opposite direction (Supplementary Section II.F). As such, Λ has a lower bound of one sperm diameter ($d \approx 0.5$–0.7 μm (refs. 19,20)), realized by a completely interdigitated arrangement of counterpropagating sperm that constitute a locally apolar material, whereas higher values of Λ reflect the copropagation of adjacent sperm, consistent with a material of higher polarity (Fig. 3e,f). We found that $\bar{\Lambda} = 1.8 \pm 1.2$ μm(Fig. 3h), comparable with the diameter of ~1–2 sperm, suggesting that the relative motion of sperm is generally that of counterpropagation, consistent with observations from photobleaching experiments in a quasi-2D geometry (Supplementary Section II.G and Supplementary Video 5). We further observed that copropagating bleached segments moved slower than their interdigitated counterparts. In particular, repetitive photobleaching of such polar regions revealed the local evolution of the sperm's relative motion, whereby polar regions became progressively apolar (Extended Data Fig. 3 and Supplementary Video 4). Although our analysis focused on regions of uniformly aligned sperm, we observe similar interdigitation of bleached flagella along director lines at topologically more complex regions like a tri-junction (Fig. 3g and Supplementary Video 4). The sperm's splitting behaviour described above is similar to that observed in densely crosslinked microtubule networks[47], but contrasts with that observed when photobleaching a dense microtubule-motor suspension (figure 2a and supplementary videos 2–4 of ref. 48), where no measurable relative sliding of microtubules is observed; instead, the photobleached region deforms with the surrounding material, stretching along the director and compressing perpendicular to it—as expected for 2D incompressible flows. Taken together, a quantitative analysis of the sperm's in vivo dynamics reveals a nematic material comprising predominantly counterpropagating flagella.

Active reptation explains observed dynamics

How might we make sense of our experimental observations? Given the sperm's dense packing and alignment in the SV, we conceived of a theoretical model in which an individual sperm's dynamics are geometrically constrained to move in an effective tube formed by its neighbours (Fig. 4a). This description is analogous to the reptation of linear polymer chains in a melt, where thermally driven transverse fluctuations along the polymer backbone are restricted to an imaginary tube[49]; here, however, the transverse undulations are generated through active bending waves along the flagellar backbone. A geometric scaling argument based on an idealized uniform packing of aligned sperm predicts that above a volume fraction of ~30%, interflagellar spacing is comparable with the amplitude of the bending waves (Supplementary Section III); given an average volume fraction of $\varphi \approx 47\%$ in the SV and the sperm's nematic alignment, wave propagation will result in contact-based interactions between adjacent flagellar backbones (Fig. 4). The deformation waves found in reconstructed sperm morphologies (Fig. 1d), the phase-synchronized waves observed among copropagating sperm within the SV (Supplementary Video 6) and the travelling bending waves moving along sperm released from the SV (Supplementary Video 1) support the thesis of flagellar wave-mediated contact interactions in vivo. Although a bacterium derives its thrust and drag from the surrounding fluid, we hypothesize that SV sperm motility stems from steric and lubrication interactions between counterpropagating flagellar bending waves. As we demonstrate below, given the sperm's dense packing in the SV, hydrodynamic interactions are heavily screened[50], suggesting that long-range fluid-mediated interactions are not central to the observed material flows.

To illustrate that contact forces between counterpropagating flagellar waves are sufficient to give rise to directed motility, we first performed simulations of interacting active filaments whose centre-line dynamics are governed by the overdamped force and moment balance as

$$\partial_s \mathbf{F} + \sum_{i \in C} \delta(s - s_c^i)\mathbf{F}_c^i + \mathbf{f}^{\mathrm{vis}} = \mathbf{0}, \tag{1}$$

$$\partial_s \mathbf{M} + \mathbf{x}_s \times \mathbf{F} + \mathbf{m}^{\mathrm{vis}} = \mathbf{0}. \tag{2}$$

The centre line $\mathbf{x}(s, t)$ is parameterized by the arc length s; $\mathbf{F}$ is the internal elastic force along the backbone and $\mathbf{M}$ is the internal bending moment; $\mathbf{F}_c^i$ is the ith contact force at the location $\mathbf{x}(s_c^i)$ from the set of $\mathcal{C}$ contacts; $\mathbf{f}^{\mathrm{vis}}$ and $\mathbf{m}^{\mathrm{vis}}$ represent viscous forces and moments per unit length, respectively. We solve the above equations within the computational framework of discrete elastic rods (DER) (Fig. 4b and Supplementary Section V.C)[51,52] in which sperm are modelled as weakly extensible filaments with an aspect ratio of 1:300 and bending rigidity of a flagellum[53]. The filaments are actuated by prescribing an internal bending moment of the form $\mathbf{M} = \mathbf{B} \cdot (\boldsymbol{\kappa} - \boldsymbol{\kappa}^{\mathrm{act}}(s, t))$, where $\mathbf{B}$ is an (isotropic) bending moduli tensor, $\boldsymbol{\kappa}$ is the instantaneous curvature vector and $\boldsymbol{\kappa}^{\mathrm{act}}(s, t)$ is a prescribed time-periodic curvature wave. The difference between the instantaneous and active curvature gives rise to moving deformation waves along the elastic filament (Supplementary Section V.C). Overlap between adjacent filaments is prevented through excluded volume interactions, modelled using soft repulsive potentials. Note that the model does not prescribe the kinematics of the filaments, but solves for the emergent dynamics. In Stokes flow, the propulsion of an isolated, undulating active filament stems from the anisotropic drag forces experienced by the slender object[54]. To preclude this mechanism of propulsion, we use isotropic drag for force $\mathbf{f}^{\mathrm{vis}}$ and torque $\mathbf{m}^{\mathrm{vis}}$ (Supplementary Section V.B); as a result, an isolated active filament does not propel (Fig. 4b(i) and Supplementary Video 6).

To investigate how contact interactions alter these dynamics in a configuration of such active, densely packed and aligned filaments, we first consider planar (2D) assemblies in two distinct arrangements. In the first, all filaments propagate waves in the same direction (Fig. 4b(ii)); in such a polar assembly, the filaments remain largely stationary (Supplementary Video 6). In the second case, neighbouring filaments propagate waves in opposite directions (Fig. 4b(iii)); in this apolar assembly, adjacent filaments translate opposite to their direction of wave propagation, resembling the experimentally observed splitting of bleached flagella in apolar regions of the SV (Fig. 3c). We also performed simulations of various configurations of filament arrangements of co- and counterpropagating filaments for quantitative comparisons with experimental data (Fig. 3c,d). Building on these findings, we next performed large-scale 3D DER simulations to explore the consequences of possible effects such as twisting, interlacing and local buckling for the two extreme cases: polar and apolar assemblies (Supplementary Section V.C). Despite these additional complexities, we observe qualitatively similar separation dynamics as in two dimensions, where filaments in an apolar configuration counterpropagate, whereas those in a polar assembly remain largely stationary (Fig. 4e).

https://doi.org/10.1038/s41567-026-03305-4

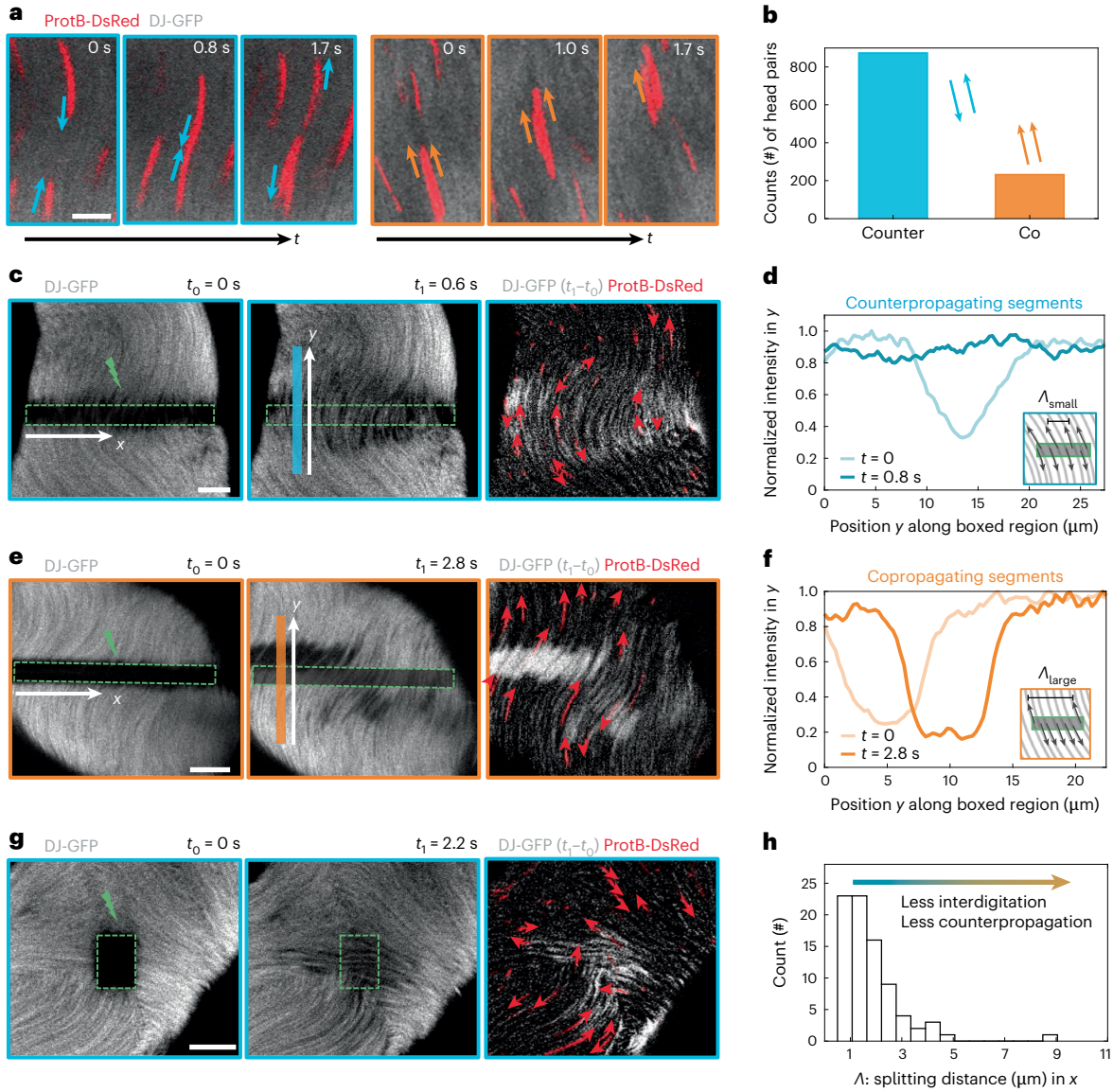

Fig. 3 | Photomanipulation experiments reveal the sperm's nematic and largely apolar arrangement. a, Snapshots from time lapses of sperm with fluorescently labelled heads (ProtB-DsRed, red) and flagella (DJ-GFP, grey) in the SV. Two contiguous pairs of heads are shown, with blue and orange arrows indicating the heads' counter- and copropagation, respectively. Scale bar, 5 μm. **b**, Bar chart of the number of such counter- and copropagating head pairs (n = 1,104 pairs from six SVs). **c**, Snapshots from the time lapse of fluorescently labelled sperm in the SV, during which a (green) rectangular ROI, perpendicular to the sperm's nematic director, is photobleached at t = 0 s. Photobleaching marks the sperm within the photobleached ROI, revealing the relative motion of flagella in this dense material. Adjacent photobleached segments counterpropagate along the nematic field lines at t = 0.6 s. The third panel shows the subtraction of the DJ-GFP signal in the two time frames to aid in visualization, with sperm heads (ProtB-DsRed) overlaid (arrows indicate their direction of motion). **d**, Normalized intensity as a function of distance in y along the blue region in **c** at t = 0 s and at t = 0.6 s, demonstrating the rapid recovery of fluorescence through the influx of unbleached sperm from above and below the bleached region in apolar regions of the material. **e**, Snapshots from a photobleaching experiment showing the splitting of the bleached region into relatively larger clusters of copropagating photobleached flagella. The third panel shows the subtraction of the DJ-GFP signal in the two time frames, with overlaid sperm heads. **f**, Normalized intensity as a function of distance along y in the orange region in **e**, at t = 2.8 s, highlighting a slower recovery of fluorescence through the influx of copropagating flagella in polar regions of the material compared with the data shown in **c** and **d**. **g**, Snapshots from an experiment in which a rectangular ROI was photobleached at a topologically complex 'tri-junctional' region, displaying qualitatively similar behaviour as that in **c**, namely, the interdigitated splitting of photobleached segments along director field lines. Scale bars, 10 μm (**c**–**g**). **h**, Histogram of Λ, a proxy for the material's local polarity, given by the distance between alternating photobleached segments travelling in the same direction, separated by single or multiple bleached segments travelling in the opposite direction ($\bar{\Lambda} = 1.8 \pm 1.2$, n = 82 from 23 photobleaching events in 15 SVs).

These results demonstrate that the reciprocal pushing of active filaments can give rise to their oppositely directed propulsion. Such counterpropagation driven by active bending waves has no direct counterpart in cytoskeletal assemblies, where sliding arises from multimeric motor proteins that drive anti-aligned filaments past one another[32,47]. The mechanism proposed here is also distinct from that of fluid-mediated thrust that drives the motility of mammalian or sea urchin sperm[54,55], but is similar to that used by other insect sperm to propel themselves through narrow ducts: rather than 'swimming freely in the seminal fluid'[46], giant sperm have been hypothesized to create a thrust to propel through contact-based interactions with the walls of the female's reproductive tract[56].

https://doi.org/10.1038/s41567-026-03305-4

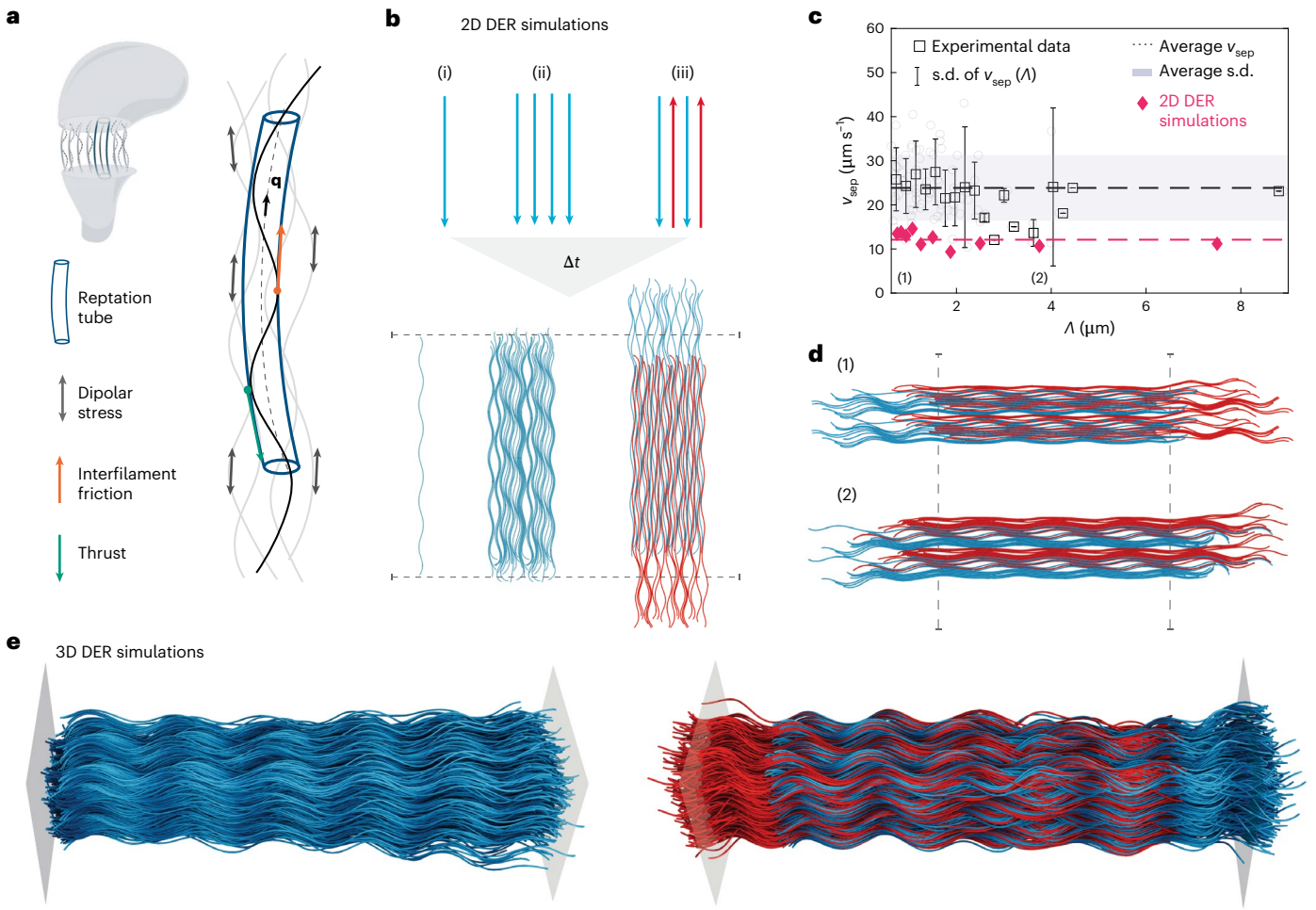

Fig. 4 | A model of reptating active filaments is supported by DER simulations and verified experimentally. a, Simplified schematic of a bisected SV showing sperm's transverse flagellar backbones and their bending waves (dashed lines). Each flagellum is constrained within a reptation tube (navy) formed by neighbouring sperm (grey), where it propagates bending waves with orientation **q**, and an amplitude comparable with the tube radius. Waves interact mechanically with those of the adjacent sperm, giving rise to propulsive thrust and interfilament friction (cyan and orange arrows, respectively). **b**, Snapshots from 2D DER simulations of active filaments in three different configurations (Supplementary Section V.B and Supplementary Video 6). The initial configurations are schematized on the top; arrows indicate the direction of wave propagation (−**q** in the hydrodynamic model). The evolved configurations are depicted in the bottom, with dashed lines indicating the initial positions of the filaments' end-points. (i) An isolated active filament simulated with isotropic drag from the surrounding medium. In the absence of anisotropic friction, the filament is immotile. (ii) An arrangement of horizontally periodic active filaments propagating bending waves in the same direction. In this polar configuration, the filaments become phase synchronized and steric interactions do not lead to directed motility. (iii) A horizontally periodic interdigitated configuration in which neighbouring filaments propagate bending waves in opposite directions. In this apolar arrangement, steric interactions lead to the counterpropagation of active filaments, as observed in photobleaching experiments of apolar regions in the SV (Fig. 3c). **c**, Plot of the separation speed v_{sep} of photobleached flagellar segments as a function of the splitting distance Λ ($n = 82$ from 23 photobleaching events in 15 SVs; values of Λ are grouped into 40 bins ranging from 0.62 to 8.9 μm; Fig. 3h). Measurements from the DER simulations are overlaid. The trends observed in the experimental and DER data are in agreement with the theoretical prediction ($v_{sep} = |\dot{\mathbf{X}}(\hat{\mathbf{s}}) - \dot{\mathbf{X}}(-\hat{\mathbf{s}})| \approx$ constant). **d**, Evolved configurations of two arrangements of interlaced active filaments corresponding to data points (1) and (2) from 2D DER simulations, with the initial positions of the filaments' end-points marked by dashed lines (Extended Data Fig. 6 and Supplementary Video 8). **e**, 3D DER simulations of polar (left) and apolar (right) configurations, performed at an experimentally comparable volume fraction of 50%, with doubly periodic boundary conditions transverse to the long axis of the undulating filaments; transparent planes mark the initial positions of the filaments' end-points.

This concept of 'moving by reciprocal pushing' leads naturally to a micro–macro continuum framework with material stresses that recapitulate the emergence of material flows in the SV. Similarly to the kinetic theory of polymeric liquids, we describe the flagellar conformation using a distribution function $\psi(\mathbf{x}, \mathbf{q}, t)$, which encodes the probability density of finding a flagellar segment with propulsive orientation $\mathbf{q} \in \mathbb{S}^2$ (the unit sphere) at location $\mathbf{x}$ (ref. 57); bending waves on a flagellar segment propagate along the propulsive orientation vector $\mathbf{q}$. The material density is $\rho(\mathbf{x}) = \int_{\mathbb{S}^2} \psi d\mathbf{q}$, and the local flagellar (or propulsive) polarity vector is $\mathbf{P}(\mathbf{x}) = \rho^{-1} \int_{\mathbb{S}^2} \mathbf{q}\psi(\mathbf{x}) d\mathbf{q}$ (with scalar order $|\mathbf{P}| \in [0, 1]$). The Fokker–Planck equation that evolves $\psi(\mathbf{x}, \mathbf{q}, t)$ depends on (1) the sperm's translational velocity $\dot{\mathbf{x}}(\mathbf{x}, \mathbf{q}, t) = \mathbf{U}(\mathbf{x}, t) + \dot{\mathbf{X}}(\mathbf{x}, \mathbf{q}, t)$, where $\mathbf{U}$ is the material flow velocity common to all flagellar segments at $\mathbf{x}$ (ref. 57) and $\dot{\mathbf{X}} = v_s[\mathbf{P} - \mathbf{q}]$ is the propulsion ('reptation') speed of individual segments (v_s is a characteristic propulsion speed, and its derivation is provided in Supplementary Section IV.B); and (2) an orientational velocity $\dot{\mathbf{q}}$, modelled using Jeffery's equation[58]—a kinematic consequence of the flagellar backbones being rotated by local gradients of the material flow (Fig. 2 and Supplementary Section IV.B).

This model makes the experimentally testable prediction that the separation speed $v_{sep} = |\dot{\mathbf{X}}(\hat{\mathbf{s}}) - \dot{\mathbf{X}}(-\hat{\mathbf{s}})|$ between oppositely directed and aligned segments of sperm is independent of the material's local

https://doi.org/10.1038/s41567-026-03305-4

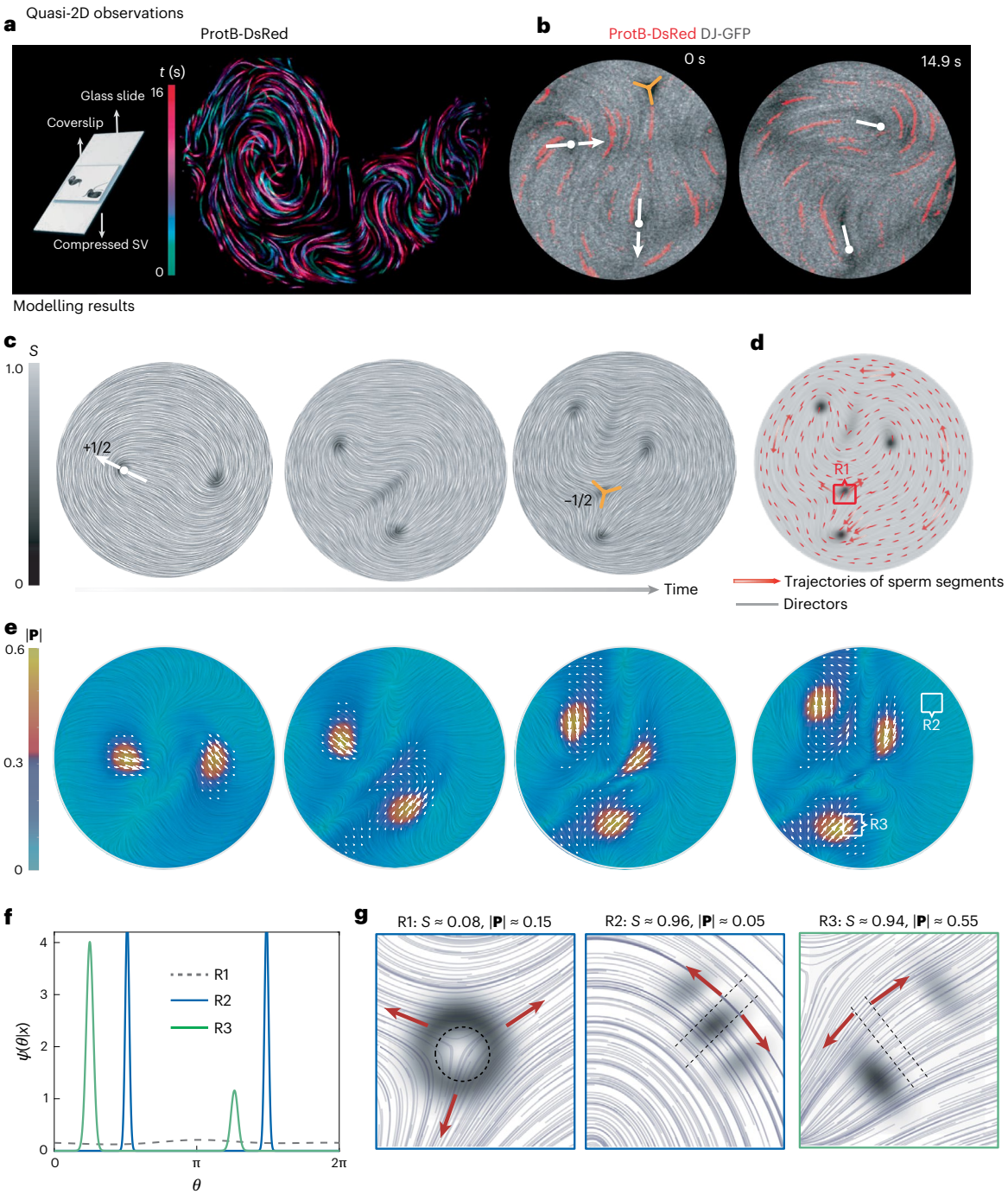

Fig. 5 | Simulations of the continuum theory reproduce in vivo spatiotemporal dynamics. a, Left: schematic of the quasi-2D experimental setup in which an SV is compressed between a coverslip and a glass slide, thereby suppressing out-of-plane motion (Extended Data Fig. 4 and Supplementary Video 5). Right: colour-coded MIP of successive frames from a time lapse of a compressed SV with fluorescently labelled sperm heads (ProtB-DsRed), demonstrating the sperm's alignment and laning behaviour, as observed in three dimensions (Fig. 2d). **b**, Live imaging of flagellar flows (DJ-GFP, grey) reveals ±1/2-order spontaneous topological defects, as also observed in three dimensions (Fig. 2a). **c**, Snapshots from simulations in a disc of the evolving director field of the flagellar material at successive time points, displayed using line integral convolution; colour encodes the nematic order parameter S. Note the continuous bending of director fields and the spontaneous emergence of ±1/2-order topological defects (Supplementary Video 9). Simulations were initiated with small perturbations to the $\mathbf{Q}$ tensor field around an aligned state; the emergent features are independent of the initial and boundary conditions (Supplementary Section IV.G). **d**, Trajectories of sperm segments (red) overlaid on the director field at a later time point, inferred from reconstructing approximations to the local distribution function $\psi(\mathbf{x}, \mathbf{q})$ (see **f**). Sperm segments in apolar ($|\mathbf{P}| \approx 0$) and nematic regions counterpropagate along the directors, whereas those in polar regions ($|\mathbf{P}| \gtrsim 0.5$) move unidirectionally in clusters. **e**, Snapshots of the associated polarity field $\mathbf{P}$, where colour encodes the strength of the local polarity $|\mathbf{P}|$. Overlaid white arrowheads highlight the average direction of polar regions. **f**, Reconstruction of the microscopic organization of the flagellar material through reconstructing $\psi(\mathbf{x}, \mathbf{q}, t)$ (Supplementary Section IV.H), where $\mathbf{q} = (\cos\theta, \sin\theta)$. $\psi(\theta|\mathbf{x})$ at a −1/2-order defect (R1), in a nematic apolar region (R2) and a nematic polar region (R3). **g**, Results from a numerical bleaching experiment on the simulated material. The bleached region is highlighted by black dashes; the black bands show the positions of the bleached regions at a later time point, and their intensity represents the density of the bleached material. Arrows indicate their direction of motion of the bleached regions; their lengths indicate their relative speeds.

polarity $\mathbf{P}(\mathbf{x}, t)$ (Supplementary Section IV.B). In contrast to $\dot{\mathbf{x}}$, which includes a contribution from the background material flow $\mathbf{U}$, v_{sep} depends only on the sperm's propulsion speed v_{s}. Using data from the photobleaching experiments, we measured the speed difference between oppositely propagating bleached sperm segments as a function of the splitting distance Λ, a proxy for the local material polarity, and found that v_{sep} is largely uncorrelated with the local polarity of the material. This trend is also in agreement with 2D DER simulations of various arrangements of co- and counterpropagating active planar filaments (Fig. 4d, Extended Data Fig. 6 and Supplementary Section V.B). Quantitative differences in the values of v_{sep} between simulation and experiment probably arise from simplifying assumptions in the DER model, such as isotropic friction, reduced filament length and the lack of details of lubrication flows (Supplementary Section V.C)

A micro–macro theory for material flows

Building on these findings, we now investigate the emergence of material flow $\mathbf{U}$ through a coarse-grained momentum balance equation:

$$-\eta\rho\mathbf{U} + \nabla\cdot\boldsymbol{\Sigma} = \mathbf{0}. \tag{3}$$

Here η is a friction coefficient and $\boldsymbol{\Sigma}$ is the coarse-grained stress tensor in the flagellar material. The total stress has four contributions $\boldsymbol{\Sigma} = \boldsymbol{\Sigma}^{\mathrm{a}} + \boldsymbol{\Sigma}^{\mathrm{el}} + \boldsymbol{\Sigma}^{\mathrm{st}} - \Pi\mathbf{I}$ (Extended Data Fig. 5). The active stress $\boldsymbol{\Sigma}^{\mathrm{a}}$, which emerges from equal and opposite frictional and contact propulsion forces, is extensile and given by $\boldsymbol{\Sigma}^{\mathrm{a}} = \alpha\rho^2(\mathbf{PP} - \mathbf{Q})$, where $\alpha > 0$ is a measure of activity and $\mathbf{Q}(\mathbf{x}) = \rho^{-1}\int_{\mathbb{S}^2}\mathbf{qq}\psi(\mathbf{x})d\mathbf{q}$ is the nematic tensor of the material. The ρ^2 dependence reflects the active stress's origins in steric interactions between counterpropagating waves. Our micro–macro framework captures the polarity dependence of this stress, such that $\boldsymbol{\Sigma}^{\mathrm{a}} \approx \mathbf{0}$ when the material is polar ($|\mathbf{P}| \approx 1$) and sperm segments are locally immotile. That $\alpha > 0$ marks the active stress as extensile, as revealed by the direction of motion of +1/2-order defects (Fig. 2g and Supplementary Video 2)[41]. The remaining stresses account for appropriate long-wavelength dynamics of elastic filaments ($\boldsymbol{\Sigma}^{\mathrm{el}}$)[59], aligning steric interactions between flagellar backbones ($\boldsymbol{\Sigma}^{\mathrm{st}}$), and incompressibility of the material flows via a Lagrange multiplier (Π) (Supplementary Section IV). A linear stability analysis around an apolar aligned state of the material predicts an instability reminiscent of the Euler buckling of elastic filaments[60] that differs from the generic bend instability of active suspensions in a Stokesian fluid[61,62] (Supplementary Section IV.E).

The first term of equation (3) reflects the dominant momentum exchange with the surrounding medium, which acts as a momentum sink. A scaling argument based on the filament packing fraction yields a hydrodynamic screening length of order $\mathcal{O}(1\,\mu\mathrm{m})$, implying that long-range hydrodynamic interactions are negligible (Supplementary Section IV). This overdamped form of the momentum balance is appropriate for capturing the dynamics observed in the live-imaging experiments of sperm in the SV, performed close to the surface (Supplementary Video 3), and in the quasi-2D coverslip experiments (Fig. 5a,b, Extended Data Fig. 4 and Supplementary Video 5); in these contexts, the sperm's organization is effectively planar and the boundaries provide drag, acting as momentum sinks (how the momentum balance is altered in the bulk is outlined in Supplementary Section IV.B). Thus, to probe the system's nonlinear dynamics, we evolve the polarity and nematic fields, $\mathbf{P}(\mathbf{x}, t)$ and $\mathbf{Q}(\mathbf{x}, t)$, respectively, in a circular disc, using a well-tested closure approximation under which the distribution function is reconstructed[63] (Supplementary Section IV).

Time evolution of the director field reveals a simulated material in a highly aligned state, whose velocity $\mathbf{U}$ is characterized by the propulsion of +1/2-order defects. We also observe the spontaneous emergence and annihilation of +1/2- and −1/2-order defect pairs in the bulk which, in a disc, preserves a topological charge of +1 (Fig. 5c and Supplementary Video 9). Simulations also provide a direct window into the evolution of the polarity field: we find that although the material is largely apolar, localized polar regions appear and disappear (Fig. 5e), and that their appearance correlates with the emergence of +1/2-order defects in the director field. For the chosen parameters (Supplementary Section IV), the model also reproduces experimentally observed correlations and statistics such as the separation of scales between defect and swimming speed, statistics of polar regions, and the correlations between material vorticity and defect speeds (Extended Data Fig. 7). Increasing the activity or the cell radius increases the number of defects observed in the system (Supplementary Section IV.I)—in agreement with studies of active nematics in confinement[40,58,64,65].

The present micro–macro framework of the coarse-grained model builds on the sperm's translational flux. Unique to this approach is now our ability to probe the microscopic organization of the flagellar material and explore the model's prediction of its dynamics. To this end, we reconstruct $\psi(\mathbf{x}, \mathbf{q}, t)$ (with $\mathbf{q} = (\cos\theta, \sin\theta)$ in two dimensions) from $\mathbf{P}(\mathbf{x}, t)$ and $\mathbf{Q}(\mathbf{x}, t)$ in three distinct regions of the material (Fig. 5f, Supplementary Video 9 and Supplementary Section IV.H)[63]. We find that in the vicinity of a −1/2-order defect, the orientational distribution of the microstructure is roughly isotropic, with $S \approx 0$, in contrast to aligned regions where $S \approx 1$. In a nematic polar region, the distribution peaks predominantly around one angle, whereas in a nematic apolar region, it peaks around two angles separated by π, corresponding to opposite orientations of the local director field. We demonstrate how this underlying microstructure influences the motion of individual sperm segments through numerical bleaching experiments (Fig. 5g). In nematic regions, sperm segments split into two counterpropagating bands along the local director, with their relative density determined by the local polarity. Thus, in apolar regions, counterpropagating bands have equal densities, whereas in polar areas, segments move unidirectionally, resembling the scenarios observed in Fig. 3c,e, respectively. In contrast with bleached segments in nematic regions, bleached segments near a −1/2-order defect split isotropically, capturing the behaviour observed experimentally when photobleaching sperm in a tri-junctional arrangement (Fig. 3g). Using the translational flux from our theory, the reconstructed distribution function at the scale of the entire material further allows us to infer the relative motion of marked sperm segments in the mass (Fig. 5d).

Discussion

Sperm, nearly universal for sexual reproduction in the animal and plant kingdoms, are among the most morphologically varying cell types, largely reflecting the various external and competitive environments in which they operate[5,7,9,10,66,67]. Still, the nature and consequences of sperm activity have been intensely studied for a few, such as mammalian and sea urchin sperm. *Drosophila*'s ultralong sperm, which arise from intense post-copulatory sexual selection[10,14,68], is a striking beyond-this-canon example. Our work establishes such giant sperm in vivo as a novel biological active matter system, whose extensile stresses arise from sperm's rapid and collective counterpropagation through densely packed storage organs. We propose that the sperm's aligned, unentangled state is maintained by these self-same stresses. We also discovered such actively reptating sperm assemblies in the female's dedicated sperm storage organs—primarily in the seminal receptacle (SR), a narrow ($d \approx 10$–30 μm) and long ($L \approx 2$ mm) blind-ended tube, where sperm can be maintained for ~2 weeks (refs. 9,13,25,26,69). By examining females mated with males with fluorescently labelled sperm, we found that consistent with previous reports (ref. 25 and supplementary video S1 of ref. 9), sperm in the SR are persistently motile (Extended Data Fig. 8 and Supplementary Video 10). Our live imaging of their flagella, however, further demonstrated that densely packed sperm are locally aligned (figs. 4d and 7d of ref. 70), and again, exhibit continuously evolving material flows, with slow-moving defects and fast counterlaning individuals (Extended Data Fig. 8 and Supplementary Video 10). These dynamics in the SR—qualitatively similar to those in the SV and following sperm deposition in the uterus as a seemingly

jumbled mass (fig. 2c of ref. 9 and fig. 4d of refs. 25,71)—further suggest a functional origin for sperm's counterpropagation within the storage organs. Taken together, these observations suggest that the emergence of collective flows is primarily associated with the dense packing of sperm, rather than the specific geometry of the confining organ. In particular, ~50% of stored sperm fertilize mature oocytes[25,26], raising questions about how sperm are extracted, almost singly, from this state[22]. Future studies of non-canonical sperm promise to reveal an expanding repertoire of behaviours and inspire inquiries at the intersection of active matter and evolution.

Active matter concepts are emerging as a powerful lens through which to study biological phenomena at the microscale[72]. Non-equilibrium dynamics driven by active extensile stresses can drive collective motion in bacterial suspensions[62], shape the mitotic spindle[73], fluidize developing epithelial tissues[61], and may drive large-scale nuclear chromatin fluctuations through the unfolding and alignment of long crumpled active polymers (fig. 3 and supplementary fig. S1 of ref. 74)[75]. Our work proposes their functional relevance to reproduction in a model organism through a distinct mechanism. Although jostled passive elastic filaments inevitably entangle under confinement[76,77], *Drosophila's* sperm avoid the dreaded knot despite their dense packing and long-term storage. We suspect that extensile active stresses arising from the sperm's persistent active reptation not only drives local nematic alignment but also generates shear via material flows that continuously reorganize neighbouring filaments, allowing them to propel past one another rather than form enduring topological constraints. This dynamic remodelling maintains the flagellar mass in an ordered and fluidized state, reminiscent of the dynamics observed in glassy active systems[78,79] and in epithelial tissues[80], suggesting a generalizable role for extensile activity in maintaining dense living matter functional.

The present continuum theory elucidates the mechanisms governing individual and collective sperm behaviours, yet it makes several simplifying assumptions. For example, we neglect non-local elastic stresses arising from tension propagation along the flagellar backbone and other effects associated with the connectivity of rod-like segments along a millimetric active filament. Further, our model does not incorporate the density fluctuations observed near defect cores. The biological phenomena described here, therefore, should inspire the development of a field-theoretic framework that integrates these features.

Last, the presence of an apolar collective state in the storage organ is notable, especially since sperm are deposited into the SV flagella first[81]. This emergent organization is probably attributable to three factors: (1) the free ends of sperm in the SV can deform at boundaries and interweave with neighbouring free ends, allowing local topological rearrangements; (2) the flexibility of the flagellum can cause localized buckling or bending, leading to in changes in motility, which we observe in male and female storage organs; and (3) the sperm's ability to propagate tip-to-base and base-to-tip bending waves[30,71]. Although not commonly observed in mammalian sperm, reversibility in wave propagation may allow ultralong sperm to reorient within narrow geometries such as the female's SR, or to detach from the common envelope embedding the heads in the male, as documented for the fruit fly *Ceratitis capitata*. The relatively short ~50-µm-long (fertile) eusperm of the gastropod *Strombus luhuanus* can also reverse—here to detach from sperm bundles or from the wall of the receptacle[37], whereas sperm of the marine worm's *Myzostoma cirriferum* do so during skin (dermal) copulation[82,83]. Despite the variety of contexts, bidirectional wave propagation imparts functional value to its practitioners.

Online content

Any methods, additional references, Nature Portfolio reporting summaries, source data, extended data, supplementary information, acknowledgements, peer review information; details of author contributions and competing interests; and statements of data and code availability are available at https://doi.org/10.1038/s41567-026-03305-4.

References

1. Taylor, V. A., Luke, B. M. & Lomas, M. B. The giant sperm of a minute beetle. *Tissue Cell* **14**, 113–123 (1982).
2. Soldatenko, E. V., Shatrov, A. B. & Petrov, A. A. Sperm packaging in the seminal vesicles of Hygrophila (Gastropoda: Pulmonata). *Zoomorphology* **137**, 367–376 (2018).
3. Smith, R. J., Matzke-Karasz, R. & Kamiya, T. Sperm length variations in five species of cypridoidean non-marine ostracods (Crustacea). *Cell Tissue Res.* **366**, 483–497 (2016).
4. Pitnick, S., Hosken, D. J. & Birkhead, T. R. in *Sperm Biology: An Evolutionary Perspective* (eds Birkhead, T. R. et al.) 69–149 (Academic Press, 2009).
5. Pitnick, S., Spicer, G. S. & Markow, T. A. How long is a giant sperm?. *Nature* **375**, 109–109 (1995).
6. Joly, D., Bressac, C. & Lachaise, D. Disentangling giant sperm. *Nature* **377**, 202–202 (1995).
7. Fitzpatrick, J. L., Kahrl, A. F. & Snook, R. R. SpermTree, a species-level database of sperm morphology spanning the animal tree of life. *Sci. Data* **9**, 30 (2022).
8. Wang, H. et al. Exceptional preservation of reproductive organs and giant sperm in Cretaceous ostracods. *Proc. R. Soc. B Biol. Sci.* **287**, 20201661 (2020).
9. Manier, M. K. et al. Resolving mechanisms of competitive fertilization success in *Drosophila melanogaster*. *Science* **328**, 354–357 (2010).
10. Miller, G. T. & Pitnick, S. Sperm-female coevolution in *Drosophila*. *Science* **298**, 1230–1233 (2002).
11. Jackson, J. A. et al. Scaling behaviour and control of nuclear wrinkling. *Nat. Phys.* **19**, 1927–1935 (2023).
12. Snook, R. R. & Hosken, D. J. Sperm death and dumping in *Drosophila*. *Nature* **428**, 939–941 (2004).
13. Bloch Qazi, M. C., Heifetz, Y. & Wolfner, M. F. The developments between gametogenesis and fertilization: ovulation and female sperm storage in *Drosophila melanogaster*. *Dev. Biol.* **256**, 195–211 (2003).
14. Lüpold, S. et al. How sexual selection can drive the evolution of costly sperm ornamentation. *Nature* **533**, 535–538 (2016).
15. Pattarini, J. M., Starmer, W. T., Bjork, A. & Pitnick, S. Mechanisms underlying the sperm quality advantage in *Drosophila melanogaster*. *Evolution* **60**, 2064–2080 (2006).
16. Bjork, A. & Pitnick, S. Intensity of sexual selection along the anisogamy-isogamy continuum. *Nature* **441**, 742–745 (2006).
17. Joly, D., Cariou, M.-L., Lachaise, D. & David, J. R. Variation of sperm length and heteromorphism in drosophilid species. *Genet. Sel. Evol.* **21**, 283–293 (1989).
18. Joly, D. & Bressac, C. Sperm length in drosophilidae (Diptera): estimation by testis and receptacle lengths. *Int. J. Insect Morphol. Embryol.* **23**, 85–92 (1994).
19. Laurinyecz, B. et al. Sperm-leucylaminopeptidases are required for male fertility as structural components of mitochondrial paracrystalline material in *Drosophila melanogaster* sperm. *PLoS Genet.* **15**, e1007987 (2019).
20. Noguchi, T., Koizumi, M. & Hayashi, S. Sustained elongation of sperm tail promoted by local remodeling of giant mitochondria in *Drosophila*. *Curr. Biol.* **21**, 805–814 (2011).
21. Perotti, M. E. The mitochondrial derivative of the spermatozoon of Drosophila before and after fertilization. *J. Ultrastruct. Res.* **44**, 181–198 (1973).
22. Tokuyasu, K. T. Dynamics of spermiogenesis in Drosophila melanogaster. *Exp. Cell Res.* **84**, 239–250 (1974).
23. Phillips, D. M. Insect sperm: their structure and morphogenesis. *J. Cell Biol.* **44**, 243–277 (1970).

24. Mencarelli, C., Lupetti, P. & Dallai, R. New insights into the cell biology of insect axonemes. *Int. Rev. Cell Mol. Biol.* **268**, 95–145 (2008).
25. Lefevre, G. & Jonsson, U. B. Sperm transfer, storage, displacement, and utilization in *Drosophila melanogaster*. *Genetics* **47**, 1719–1736 (1962).
26. Kaufman, B. P. & Demerec, M. Utilization of sperm by the female Drosophila melanogaster. *Am. Nat.* **76**, 445–469 (1942).
27. Tram, U. & Wolfner, M. F. Male seminal fluid proteins are essential for sperm storage in *Drosophila melanogaster*. *Genetics* **153**, 837–844 (1999).
28. Lieberman-Aiden, E. et al. Comprehensive mapping of long-range interactions reveals folding principles of the human genome. *Science* **326**, 289–293 (2009).
29. Patil, V. P. et al. Ultrafast reversible self-assembly of living tangled matter. *Science* **380**, 392–398 (2023).
30. Yang, Y. & Lu, X. Drosophila sperm motility in the reproductive tract. *Biol. Reprod.* **84**, 1005–1015 (2011).
31. Lu, X. Fluorescent imaging of *Drosophila melanogaster* sperm in the reproductive tract: a new model of flagellar motility. *Methods Enzymol.* **525**, 131–148 (2013).
32. Sanchez, T., Chen, D. T. N., DeCamp, S. J., Heymann, M. & Dogic, Z. Spontaneous motion in hierarchically assembled active matter. *Nature* **491**, 431–434 (2012).
33. Zhou, S., Sokolov, A., Lavrentovich, O. D. & Aranson, I. S. Living liquid crystals. *Proc. Natl Acad. Sci. USA* **111**, 1265–1270 (2014).
34. Denk, W. & Horstmann, H. Serial block-face scanning electron microscopy to reconstruct three-dimensional tissue nanostructure. *PLoS Biol.* **2**, e329 (2004).
35. Santel, A., Blümer, N., Kämpfer, M. & Renkawitz-Pohl, R. Flagellar mitochondrial association of the male-specific Don Juan protein in Drosophila spermatozoa. *J. Cell Sci.* **111**, 3299–3309 (1998).
36. Jayaramaiah Raja, S. & Renkawitz-Pohl, R. Replacement by Drosophila melanogaster protamines and mst77f of histones during chromatin condensation in late spermatids and role of sesame in the removal of these proteins from the male pronucleus. *Mol. Cell. Biol.* **25**, 6165–6177 (2005).
37. Shiba, K., Shibata, D. & Inaba, K. Autonomous changes in the swimming direction of sperm in the gastropod *Strombus luhuanus*. *J. Exp. Biol.* **217**, 986–996 (2014).
38. Donato, C. C., Gomes, M. A. F. & de Souza, R. E. Crumpled wires in two dimensions. *Phys. Rev. E* **66**, 015102 (2002).
39. Faluweki, M. K., Cammann, J., Mazza, M. G. & Goehring, L. Active spaghetti: collective organization in cyanobacteria. *Phys. Rev. Lett.* **131**, 158303 (2023).
40. Norton, M. M. et al. Insensitivity of active nematic liquid crystal dynamics to topological constraints. *Phys. Rev. E* **97**, 012702 (2018).
41. Copenhagen, K., Alert, R., Wingreen, N. S. & Shaevitz, J. W. Topological defects promote layer formation in Myxococcus xanthus colonies. *Nat. Phys.* **17**, 211–215 (2021).
42. Kawaguchi, K., Kageyama, R. & Sano, M. Topological defects control collective dynamics in neural progenitor cell cultures. *Nature* **545**, 327–331 (2017).
43. Doostmohammadi, A., Ignés-Mullol, J., Yeomans, J. M. & Sagués, F. Active nematics. *Nat. Commun.* **9**, 3246 (2018).
44. Bressac, C. et al. Comparative kinetics of short and long sperm in sperm dimorphic Drosophila species. *Cell Motil.* **19**, 269–274 (1991).
45. Tokuyasu, K. T., Peacock, W. J. & Hardy, R. W. Dynamics of spermiogenesis in Drosophila melanogaster: II. Coiling process. *Z. Zellforsch. Mikrosk. Anat.* **127**, 492–525 (1972).
46. Werner, M., Gack, C., Speck, T. & Peschke, K. Queue up, please! Spermathecal filling in the rove beetle Drusilla canaliculata (Coleoptera, Staphylinidae). *Naturwissenschaften* **94**, 837–841 (2007).
47. Fürthauer, S. et al. Self-straining of actively crosslinked microtubule networks. *Nat. Phys.* **15**, 1295–1300 (2019).
48. Lemma, L. M. et al. Multiscale microtubule dynamics in active nematics. *Phys. Rev. Lett.* **127**, 148001 (2021).
49. de Gennes, P.-G. Reptation of a polymer chain in the presence of fixed obstacles. *J. Chem. Phys.* **55**, 572–579 (1971).
50. Muthukumar, M. & Edwards, S. F. Screening concepts in polymer solution dynamics. *Polymer* **23**, 345–348 (1982).
51. Bergou, M., Wardetzky, M., Robinson, S., Audoly, B. & Grinspun, E. Discrete elastic rods. In *ACM SIGGRAPH 2008 Papers* 1–12 (ACM, 2008).
52. Vetter, R., Wittel, F. K. & Herrmann, H. J. Packing of elastic wires in flexible shells. *Europhys. Lett.* **112**, 44003 (2015).
53. Rikmenspoel, R. Movements and active moments of bull sperm flagella as a function of temperature and viscosity. *J. Exp. Biol.* **108**, 205–230 (1984).
54. Gray, J. & Hancock, G. J. The propulsion of sea-urchin spermatozoa. *J. Exp. Biol.* **32**, 802–814 (1955).
55. Li, C., Chakrabarti, B., Castilla, P., Mahajan, A. & Saintillan, D. Chemomechanical model of sperm locomotion reveals two modes of swimming. *Phys. Rev. Fluids* **8**, 113102 (2023).
56. Demerec, M. (ed.) *Biology of Drosophila* (Cold Spring Harbor Laboratory Press, 1994).
57. Doi, M. & Edwards, S. F. *The Theory of Polymer Dynamics* Vol. 73 (Oxford Univ. Press, 1988).
58. Gao, T., Betterton, M. D., Jhang, A.-S. & Shelley, M. J. Analytical structure, dynamics, and coarse graining of a kinetic model of an active fluid. *Phys. Rev. Fluids* **2**, 093302 (2017).
59. de Gennes, P.-G. & Prost, J. *The Physics of Liquid Crystals* (Oxford Univ. Press, 1993).
60. Audoly, B. & Pomeau, Y. in *Peyresq Lectures on Nonlinear Phenomena* 1–35 (World Scientific, 2000).
61. Simha, R. A. & Ramaswamy, S. Hydrodynamic fluctuations and instabilities in ordered suspensions of self-propelled particles. *Phys. Rev. Lett.* **89**, 058101 (2002).
62. Saintillan, D. & Shelley, M. J. Instabilities and pattern formation in active particle suspensions: kinetic theory and continuum simulations. *Phys. Rev. Lett* **100**, 178103 (2008).
63. Weady, S., Stein, D. B. & Shelley, M. J. Thermodynamically consistent coarse-graining of polar active fluids. *Phys. Rev. Fluids* **7**, 063301 (2022).
64. Opathalage, A. et al. Self-organized dynamics and the transition to turbulence of confined active nematics. *Proc. Natl Acad. Sci. USA* **116**, 4788–4797 (2019).
65. Joshi, C. et al. From disks to channels: dynamics of active nematics confined to an annulus. *Soft Matter* **19**, 5630–5640 (2023).
66. PARKER, G. A. Sperm competition and its evolutionary consequences in the insects. *Biol. Rev.* **45**, 525–567 (1970).
67. Parker, G. A. Conceptual developments in sperm competition: a very brief synopsis. *Philos. Trans. R. Soc. B Biol. Sci.* **375**, 20200061 (2020).
68. Syed, Z. A. et al. Genomics of a sexually selected sperm ornament and female preference in Drosophila. *Nat. Ecol. Evol.* **9**, 336–348 (2024).
69. Neubaum, D. M. & Wolfner, M. F. Mated *Drosophila melanogaster* females require a seminal fluid protein, acp36de, to store sperm efficiently. *Genetics* **153**, 845–857 (1999).
70. Zelinger, E. et al. Three-dimensional correlative microscopy of the Drosophila female reproductive tract reveals modes of communication in seminal receptacle sperm storage. *Commun. Biol.* **7**, 155 (2024).
71. Köttgen, M. et al. Drosophila sperm swim backwards in the female reproductive tract and are activated via TRPP2 ion channels. *PLoS ONE* **6**, e20031 (2011).

72. Needleman, D. & Dogic, Z. Active matter at the interface between materials science and cell biology. *Nat. Rev. Mater.* **2**, 17048 (2017).
73. Brugués, J. & Needleman, D. Physical basis of spindle self-organization. *Proc. Natl Acad. Sci. USA* **111**, 18496–18500 (2014).
74. Saintillan, D., Shelley, M. J. & Zidovska, A. Extensile motor activity drives coherent motions in a model of interphase chromatin. *Proc. Natl Acad. Sci. USA* **115**, 11442–11447 (2018).
75. Mahajan, A., Yan, W., Zidovska, A., Saintillan, D. & Shelley, M. J. Euchromatin activity enhances segregation and compaction of heterochromatin in the cell nucleus. *Phys. Rev. X* **12**, 041033 (2022).
76. Belmonte, A., Shelley, M. J., Eldakar, S. T. & Wiggins, C. H. Dynamic patterns and self-knotting of a driven hanging chain. *Phys. Rev. Lett.* **87**, 114301 (2001).
77. Raymer, D. M. & Smith, D. E. Spontaneous knotting of an agitated string. *Proc. Natl Acad. Sci. USA* **104**, 16432–16437 (2007).
78. Bi, D., Yang, X., Marchetti, M. C. & Manning, M. L. Motility-driven glass and jamming transitions in biological tissues. *Phys. Rev. X* **6**, 021011 (2016).
79. Mandal, R., Bhuyan, P. J., Chaudhuri, P., Dasgupta, C. & Rao, M. Extreme active matter at high densities. *Nat. Commun.* **11**, 2581 (2020).
80. Rozman, J. & Yeomans, J. M. Cell sorting in an active nematic vertex model. *Phys. Rev. Lett* **133**, 248401 (2024).
81. Dubey, P., Shirolikar, S. & Ray, K. Localized, reactive F-actin dynamics prevents abnormal somatic cell penetration by mature spermatids. *Dev. Cell* **38**, 507–521 (2016).
82. Ishijima, S., Ishijima, S. A. & Afzelius, B. A. Movement of *Myzostomum* spermatozoa: calcium ion regulation of swimming direction. *Cell Motil.* **28**, 135–142 (1994).
83. Afzelius, B. A. The spermatozoon of Myzostomum cirriferum (Annelida, Myzostomida). *J. Ultrastruct. Res.* **83**, 58–68 (1983).

Methods

Detailed descriptions of experimental methods, image processing, simulations and theory are provided in the Supplementary Information.

Experiments

To study sperm with fluorescently labelled heads (ProtB-DsRed) and tails (DJ-GFP) in the male and female storage organs, that is, the SV and the SR, respectively, were extracted through dissection in ~200 µl of Schneider's medium and placed in a glass-bottom dish with a lid to prevent drying. To release sperm into the medium, a thin needle was used to rupture the storage organs. Dissected SVs with fluorescently labelled sperm were fixed in 4% (wt/vol) paraformaldehyde for 3D confocal imaging. To reduce the sperm's dynamics to quasi-two dimensions, the storage organs were transferred to a glass slide and covered with an 18 × 18-mm^2 #1.5 coverslip. Confocal microscopy data were acquired using the Nikon AX R laser scanning confocal microscope, and the NIS-Elements software (v6.20.02 64-bit), using a ×20/0.75 air or ×40/1.25 silicon objective. Serial block-face imaging of the resin-embedded SV was performed using a Gatan OnPoint BSE detector in a ZEISS GEMINI 300 VP FESEM device equipped with a Gatan 3View automatic microtome unit. Data acquisition settings and stage control were performed using the Gatan DigitalMicrograph software (v. 3.31).

Image analysis

Fiji[84] and MATLAB[85] were used to analyse the data and generate the plots. Analysis of the SBF-SEM data was performed using Dragonfly 4.1 (ref. 86). 3D visualizations of the SBF-SEM data were generated in ParaView (v5.11.2)[87,88]. Nematic director lines were computed from confocal images of fluorescently labelled sperm heads (ProtB-DsRed). The computations were performed in MATLAB 2024 and closely followed the algorithm outlined in refs. 89–91. To compute the material flow field from live-imaging data, we performed optical flow analysis on the confocal time lapses of SVs with fluorescently labelled sperm tails (DJ-GFP), using open-source MATLAB 2019 codes[92] that implement the algorithm outlined in ref. 93. Measurements of average sperm orientation in the SV were performed using FibrilTool Batch[94,95], which computes the average orientation of fibrillar arrays.

Simulations

To perform DER simulations, each fibre was represented as a sequence of straight segments joined at nodes, with nodal positions providing the sole degrees of freedom. Geometric quantities such as segment lengths, tangents and curvatures were derived from this centre-line discretization. To resolve curvature with sign and frame consistency, we adopted a quaternion-based material frame on each segment, following the formalism of ref. 96. Together with weakly inextensible backbone springs and Hertzian repulsion between non-adjacent segments, this formulation captured the essential mechanical ingredients of undulatory motion. Time integration was performed using the explicit Euler scheme. Details of the implementation are provided in Supplementary Section V. To understand how active stresses give rise to emergent material flows in the SV, we performed direct numerical simulations of the coarse-grained continuum model inside a disc (Supplementary Section IV). Briefly, we evolved the polarity and nematic tensor fields $\mathbf{P}(\mathbf{x}, t)$ and $\mathbf{Q}(\mathbf{x}, t)$, respectively, using a spectral solver, Dedalus[97]. For time marching, we used an exponential integrator coupled with a fourth-order accurate Runge–Kutta scheme with adaptive time stepping.

Data availability

All data that support the plots and other findings of this study are available from the corresponding author upon reasonable request.

Code availability

The computational methods are further described in the Supplementary Information and the associated code is available via GitHub at https://github.com/flatironinstitute/alsous_gigantism_2025.

References

84. Schindelin, J. et al. Fiji: an open-source platform for biological-image analysis. *Nat. Methods* **9**, 676–682 (2012).
85. MATLAB version: 9.13.0 (R2022b) (The MathWorks Inc., 2022).
86. Dragonfly 2022.2 (Object Research Systems, 2022).
87. Ahrens, J., Geveci, B. & Law, C. *ParaView: An End-User Tool for Large Data Visualization*. Visualization Handbook. (Elsevier, 2005).
88. Ayachit, U. *The ParaView Guide: A Parallel Visualization Application* (Kitware, 2015).
89. Tan, A. J. et al. Topological chaos in active nematics. *Nat. Phys.* **15**, 1033–1039 (2019).
90. Ellis, P. W. et al. Curvature-induced defect unbinding and dynamics in active nematic toroids. *Nat. Phys.* **14**, 85–90 (2018).
91. Blackwell, R. et al. Microscopic origins of anisotropic active stress in motor-driven nematic liquid crystals. *Soft Matter* **12**, 2676–2687 (2016).
92. Black, M. J. Optical flow code and datasets. https://cs.brown.edu/people/mjblack/code.html (accessed 26 December 2024).
93. Sun, D., Roth, S. & Black, M. J. Secrets of optical flow estimation and their principles. In *Proc. IEEE Computer Society Conference on Computer Vision and Pattern Recognition* 2432–2439 (IEEE, 2010).
94. Boudaoud, A. et al. Fibriltool, an ImageJ plug-in to quantify fibrillar structures in raw microscopy images. *Nat. Protoc.* **9**, 457–463 (2014).
95. Louveaux, M. & Boudaoud, A. FibrilTool Batch: an automated version of the ImageJ/Fiji plugin FibrilTool. *Zenodo* https://doi.org/10.5281/zenodo.2528872 (2018).
96. Körner, K., Audoly, B. & Bhattacharya, K. Simple deformation measures for discrete elastic rods and ribbons. *Proc. R. Soc. A Math. Phys. Eng. Sci.* **477**, 20210561 (2021).
97. Burns, K. J., Vasil, G. M., Oishi, J. S., Lecoanet, D. & Brown, B. P. Dedalus: a flexible framework for numerical simulations with spectral methods. *Phys. Rev. Res.* **2**, 023068 (2020).

Acknowledgements

We thank A. Liang and J. Sall of the NYULH DART Microscopy Lab for assistance with electron microscopy, supported by Cancer Center Grant P30CA016087; the Gemini300SEM with 3View was purchased with NIH S10 OD019974. B.C. acknowledges support from the Department of Atomic Energy, Government of India (under project number RTI4019). We are grateful to K. Fan and S. Zhang for help with sperm tracking from the SBF-SEM data; J. Jackson (MPI-CG) and N. Romeo (U. Chicago) for image analysis assistance; and S. Weady, R. Farhadifar, S. Shvartsman (all Flatiron Institute), F. Jülicher (MPI-CS), M. Rao (NCBS) and D. Fisher (Stanford University) for valuable discussions. Computations were carried out at the Flatiron Institute's Scientific Computing Core (SCC). Confocal microscopy was performed at the CCBScope Observatory in the Center for Computational Biology (CCB) at the Flatiron Institute.

Author contributions

J.I.A. conceived the project. J.I.A. designed and conducted the experiments with input from B.C. and M.J.S. B.C. and M.J.S. developed the theoretical model and implemented the continuum simulations. B.P. performed the DER simulations and developed the data visualization framework for Fig. 1. J.I.A. and B.C. performed the image and data analyses. J.I.A. and B.C. wrote the original manuscript with input from all authors. All authors reviewed the manuscript.

Competing interests
The authors declare no competing interests.

Additional information
Extended data is available for this paper at https://doi.org/10.1038/s41567-026-03305-4.

Supplementary information The online version contains supplementary material available at https://doi.org/10.1038/s41567-026-03305-4.

Correspondence and requests for materials should be addressed to Michael J. Shelley.

Peer review information *Nature Physics* thanks K. R. Prathyusha, Reza Nosrat and Daiki Nishiguchi for their contribution to the peer review of this work.

https://doi.org/10.1038/s41567-026-03305-4

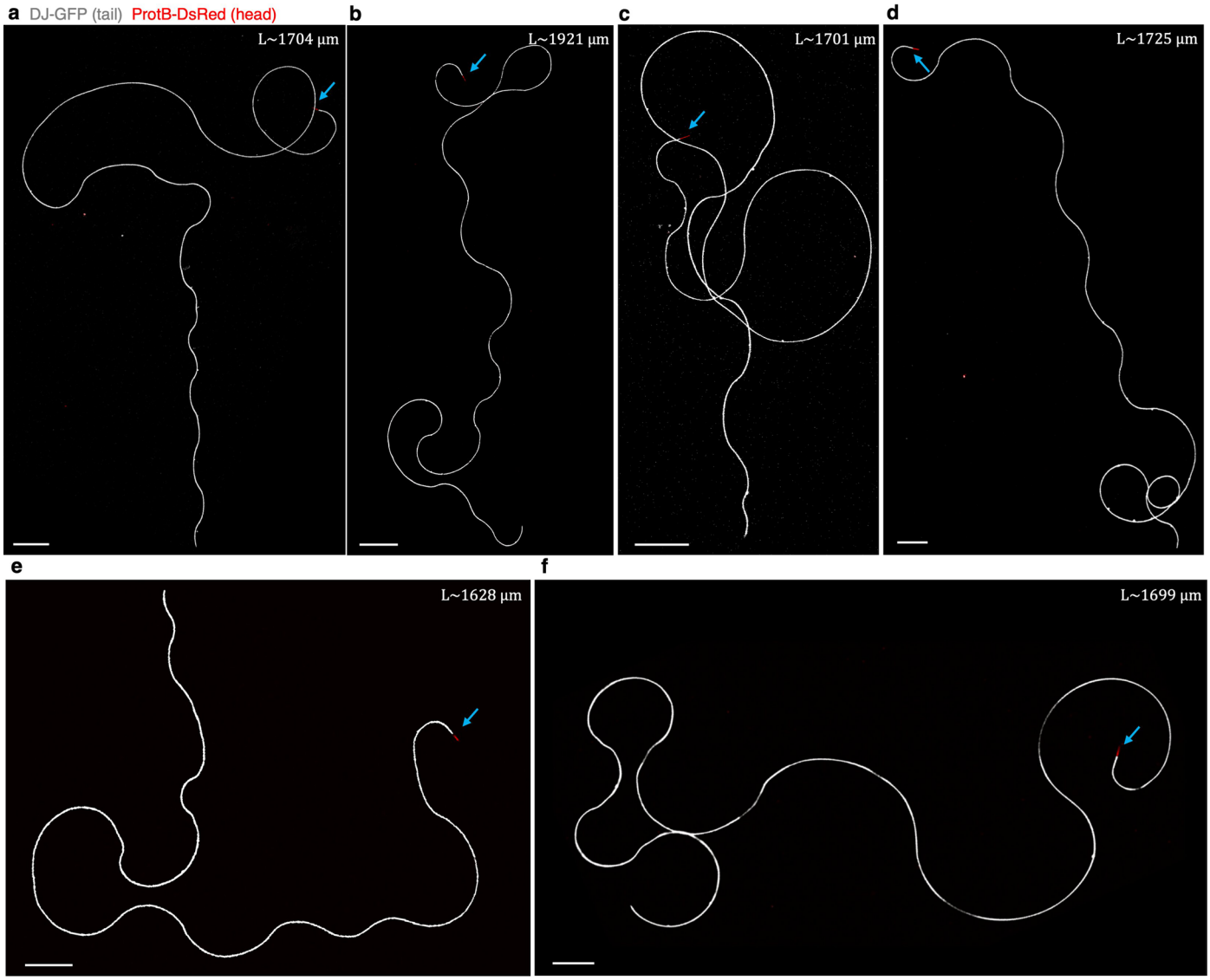

Extended Data Fig. 1 | Confocal microscopy images of individual *Drosophila melanogaster* sperm. a-f: Examples of individual sperm with fluorescently labeled flagella (that is, tails) (DJ-GFP) and heads (ProtB-DsRed), extracted from the male's storage organ, the seminal vesicle (SV). Sperm lengths, in μm, are shown; blue arrow points to each sperm's head. Measured sperm lengths are consistent with those reported in[18], where sperm lengths were estimated by measuring the lengths of individual sperm and of sperm within mature cysts in the testes. The sperm in **f** was used to generate the outline of the sperm in Fig. 1a of the main text. Scale bars = 50 μm.

https://doi.org/10.1038/s41567-026-03305-4

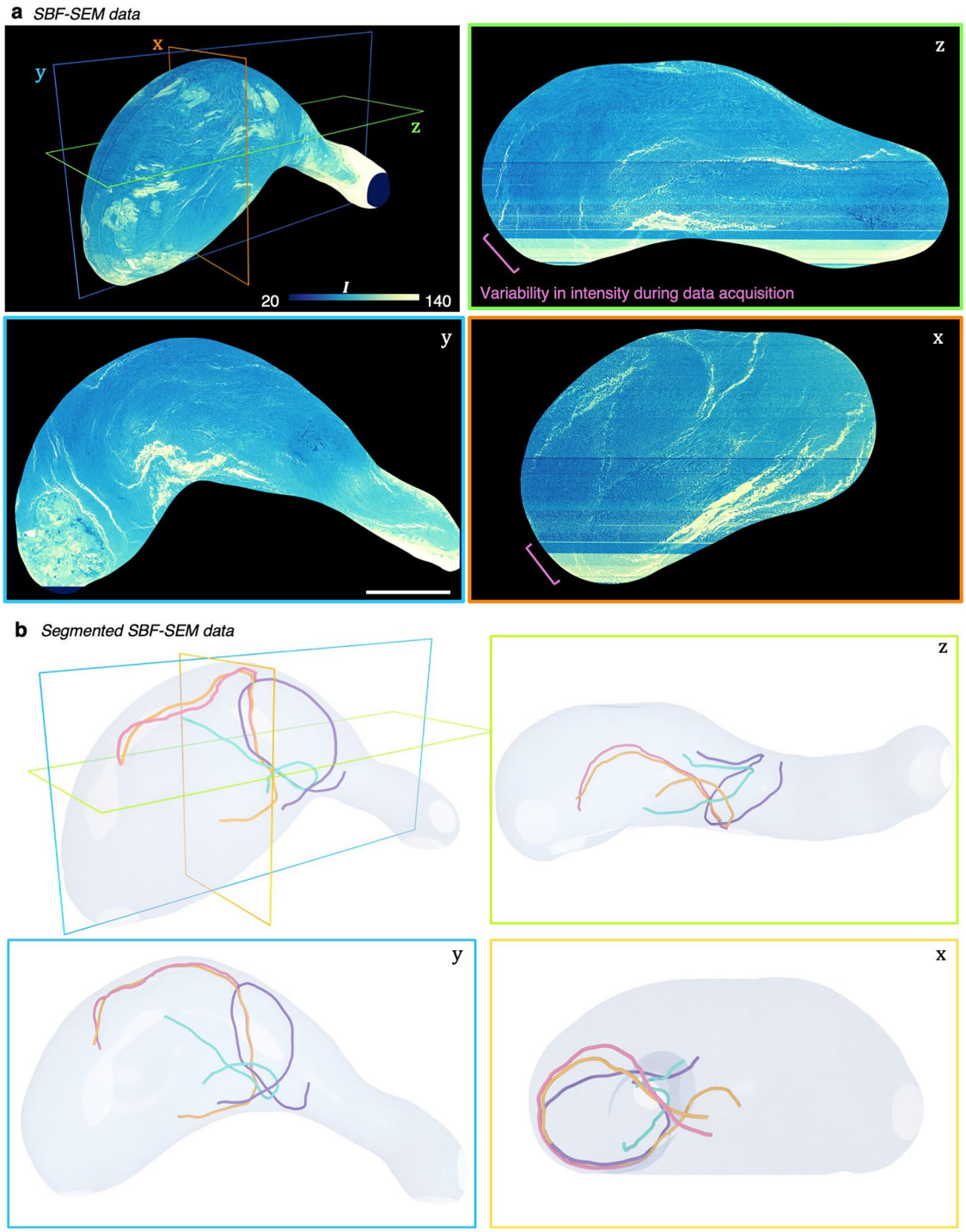

Extended Data Fig. 2 | Reconstructions of sperm from serial block-face scanning electron microscopy (SBF-SEM) data. a, A 3D rendered image of sperm in the SV, colored by intensity *I*, acquired through SBF-SEM (Supplementary Video 2). Several cross-sectional views are shown; note the dense and aligned packing of sperm throughout the SV. The observed variation in intensity arises from variability in the microscope and camera settings during data acquisition. Scale bar = 50 μm. **b**, 3D rendered image of the reconstructed SV showing four partially segmented sperm based on SBF-SEM data (Fig. S3). Sperm were segmented manually by tracking and highlighting the sperm's cross sectional area in successive slices using Dragonfly 4.1. Figure 1d,e in the main text show these segmented sperm overlaid with the SBF-SEM data of the entire SV. Also shown are different color-coded views of the SV and segmented sperm. The visualizations were generated in ParaView.

https://doi.org/10.1038/s41567-026-03305-4

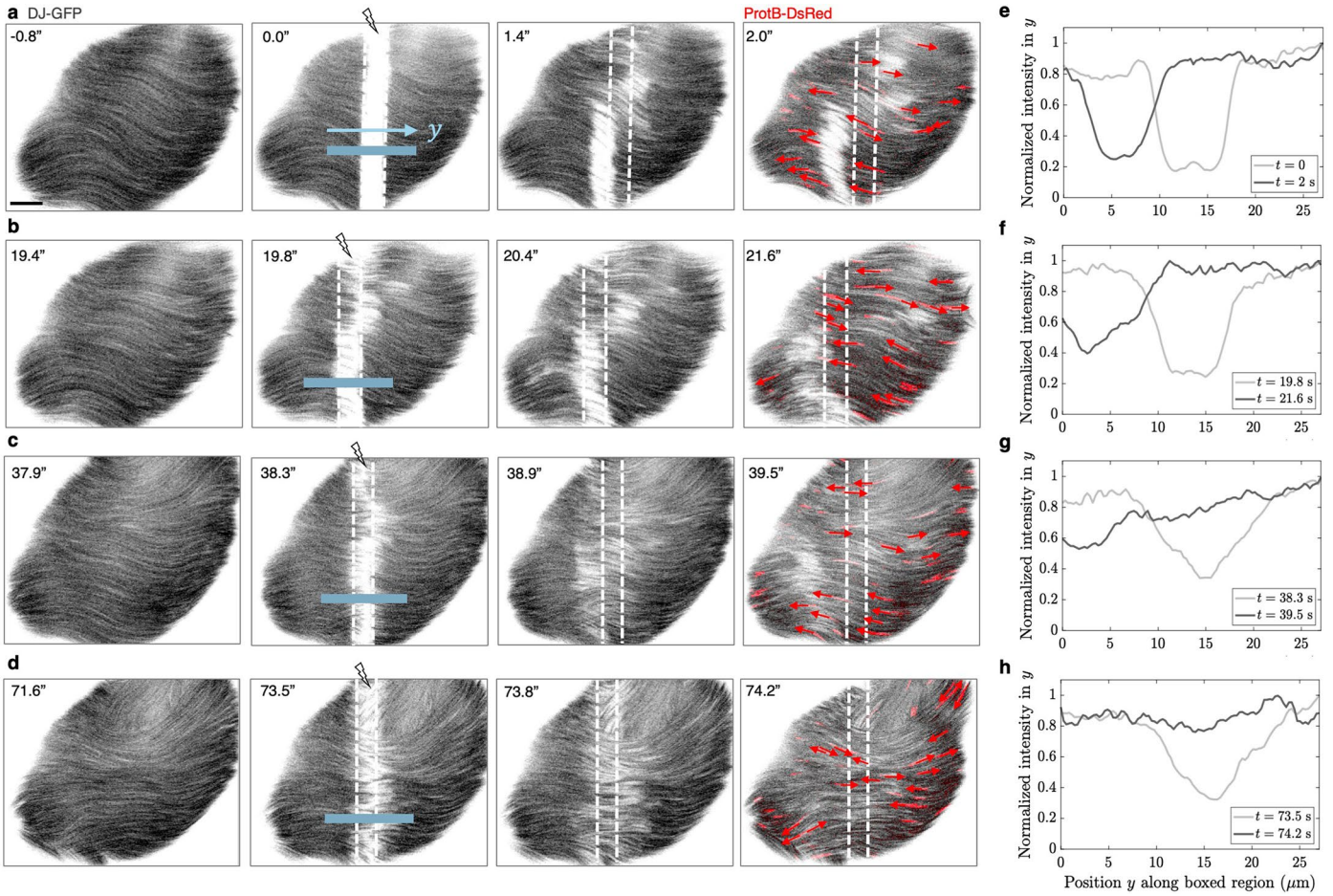

Extended Data Fig. 3 | Photobleaching experiments reveal the evolution of the material's polarity field and organization. a-d Snapshots from a time lapse of sperm with fluorescently labeled flagella (DJ-GFP) and heads (ProtB-DsRed) in the SV, showing recovery of fluorescence and evolution of the material's polarity after four successive photobleaching events ($t = 0$ s, $t = 19.8$ s, $t = 38.3$ s, $t = 73.5$ s). A bleach line, transverse to the sperm's nematic director, is demarcated by dashed white lines. Sperm heads and their direction of propagation (arrows) are shown in the final time point of each bleach event. **e-h**, Normalized intensity as a function of distance along the highlighted band (blue) at bleaching and at a subsequent time point. As seen from the timelapses and the adjoining quantification, the material's polarity evolves. Scale bar = 10 μm.

https://doi.org/10.1038/s41567-026-03305-4

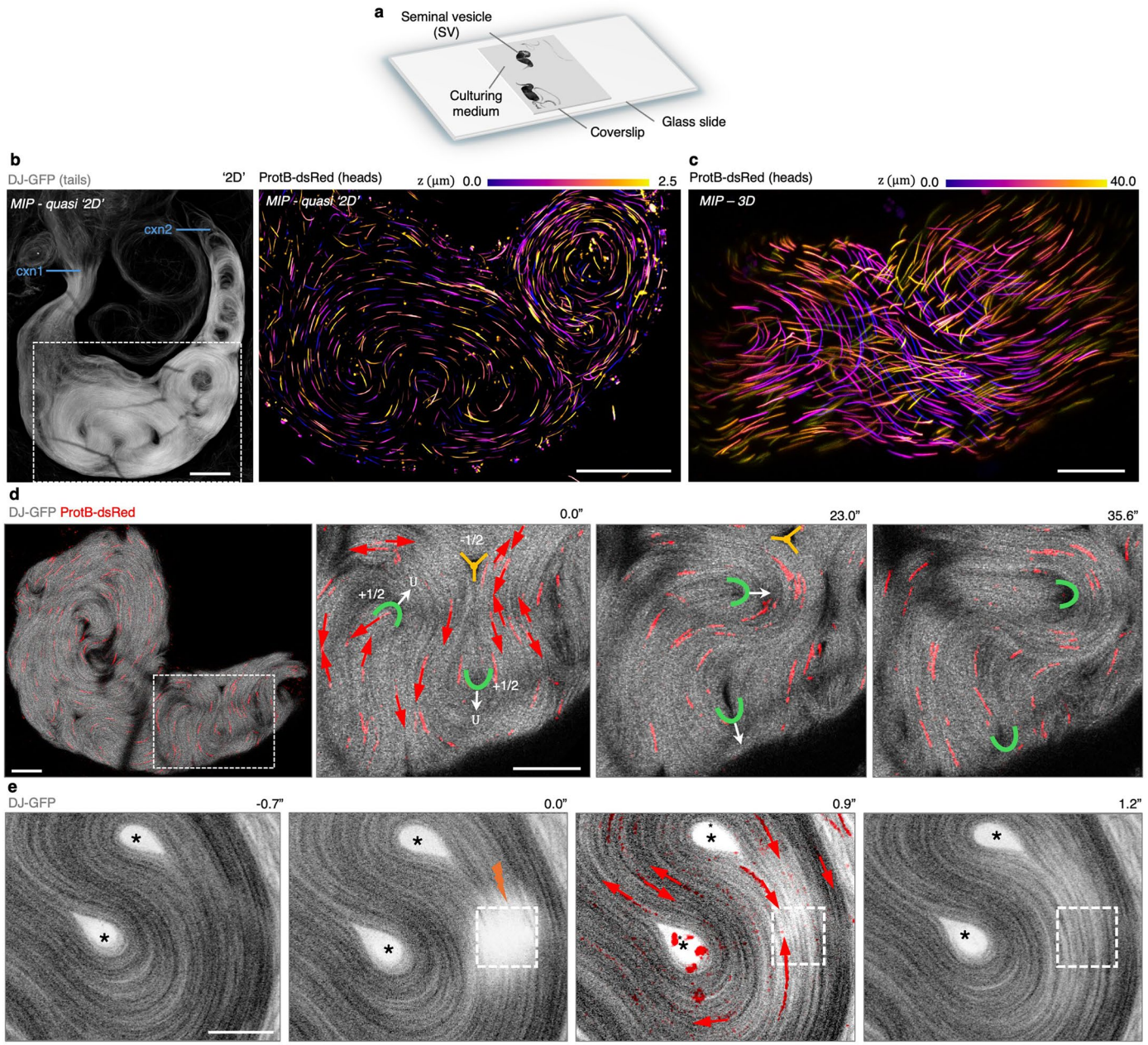

Extended Data Fig. 4 | Features of 3D spatiotemporal dynamics largely preserved in compressed quasi-2D samples. a, Schematic of the experimental setup. Dissected SVs in Schneider's medium were aspirated using a pipette with a cut tip, placed on a glass slide, and compressed with a coverslip that was partially sealed (two sides) with clear nail polish. **b**,*(Left)* Confocal image of fluorescently labeled sperm (DJ-GFP) in a SV disconnected from the testis (cxn1) and the ejaculatory duct (cxn2) under a coverslip. In this experimental setup, the SV is compressed, causing rapid exit of sperm from the severed ends. The remaining sperm are confined to a ~ 3 – 5 μm depth; this configuration is thus referred to as quasi-2D. *(Right)* Maximum intensity projection (MIP) of sperm heads in the boxed region in **a**, demonstrating the absence of variation in the material's director field in z - as opposed to the 3D case of an uncompressed SV shown in **c**, and in Fig. 1d,f in the main text. Scale bars in left and right panels = 50 μm. **c**, 3D-rendered image of a z-stack of an uncompressed SV. Note the varying orientations of sperm heads, a proxy for material organization, as a function of depth through this portion of the storage organ (color encodes position in z in μm). Scale bar = 20 μm. **d**, Snapshots from a time series of the boxed region of a compressed SV, highlighting two + 1/2- and – 1/2-order defects. Arrows overlaid on the sperm heads (ProtB-DsRed) indicate the direction of propagation of individual sperm. Scale bars = 20 μm. **e**, Snapshots from a time lapse in a compressed SV, in which a rectangular region (10 μm x 10 μm) in the SV was photobleached at t = 0 s. Subsequent time frames show the counter-propagation of sperm and eventual recovery of fluorescence through the influx of counter-propagating sperm. Stars indicate the positions of +1/2-order defects that are devoid of sperm. Scale bar = 10 μm.

https://doi.org/10.1038/s41567-026-03305-4

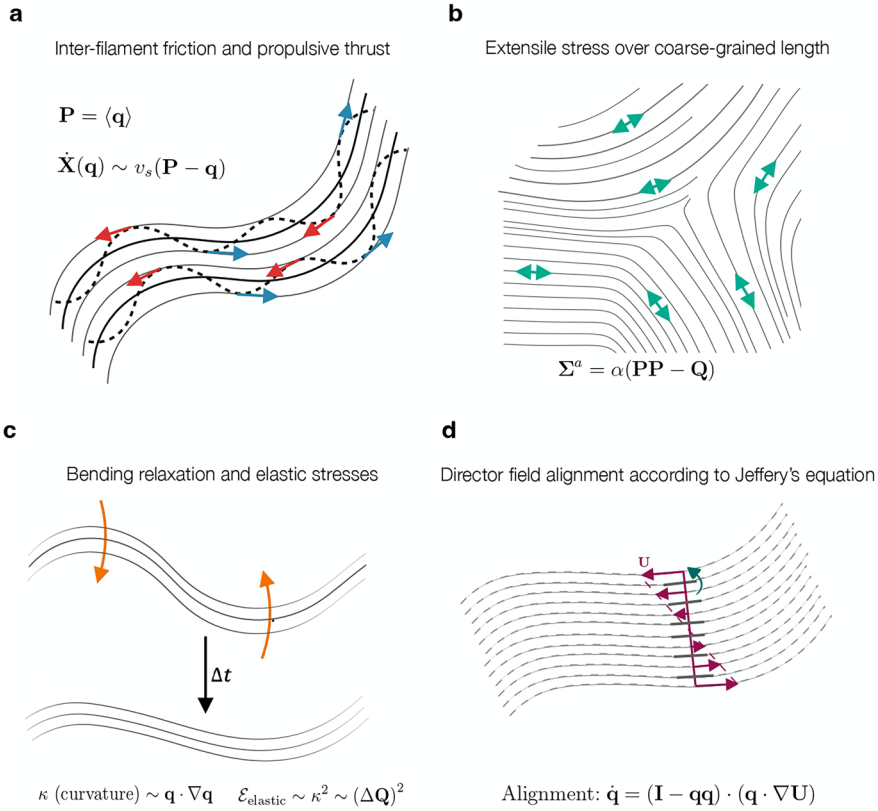

Extended Data Fig. 5 | Schematics of the mechanical interactions that form the basis of the micro-macro theory. a, Inter-filament friction (red arrows) and thrust (blue arrows) forces resulting from mechanical interaction between bending waves (dashed lines) in the sperm assembly. The net propulsive thrust and, in turn, $\dot{\mathbf{X}}(\mathbf{q})$, depend on the local polarity $\mathbf{P}(\mathbf{x})$ of the material. The model neglects the role of possible phase-synchronization in neighboring waves. **b**, The contact interactions that give rise to directed motility also lead to extensile stresses over length scales much larger than those over which contact interactions occur. These dipolar stresses (double-headed arrows) depend on the nematic tensor **Q** and the polarity field **P**. **c**, Field theoretical description of elasticity in aligned fibers that mimic the passive bending relaxation of sperm segments. **d**, Alignment and rotation of sperm segments with the mean-field material flow **U** (portrayed as a shear flow using purple arrows). The green arrow indicates the rotation of sperm segments.

https://doi.org/10.1038/s41567-026-03305-4

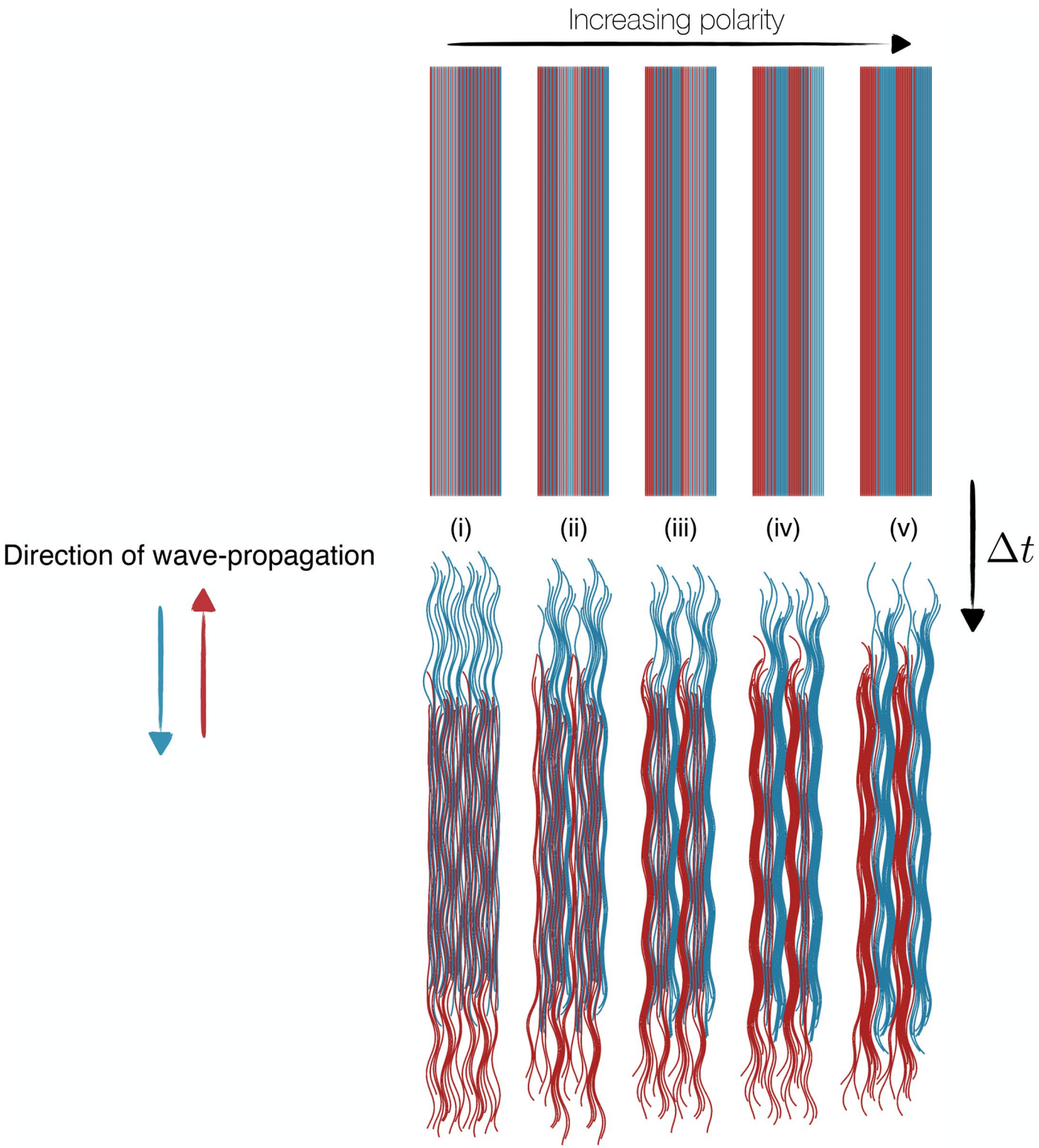

Extended Data Fig. 6 | Discrete Elastic Rod (DER) simulations of active filaments in various interleaved configurations. Active filaments are interleaved to various extents. The polarity of these configurations increases from left to right (top row arrow). The polar configurations can be associated with coherently moving groups of sperm with high Λ in the experiments. The bottom row highlights the splitting dynamics of the configurations at a later time point. The aspect ratio 300 filaments are modeled using $N = 300$ weakly extensible segments with linear elastic stretching (along each segment) and bending rigidity (between adjacent segments) comparable to that of a bull sperm flagella[53]. Undulatory motion is driven by a time-varying sinusoidal rest curvature with five periods of osculation long each filament and a random phase shift per filament to desynchronize the initial state. The evolution of the filaments is governed by isotropic passive drag from the suspending fluid, chosen such that isolated filaments do not self-propel. Each of these five simulations contains 20 filaments—10 propagating waves downward and 10 propagating waves upward—at an area fraction of 80% with periodic boundary conditions transverse to the long axis of the filaments.

https://doi.org/10.1038/s41567-026-03305-4

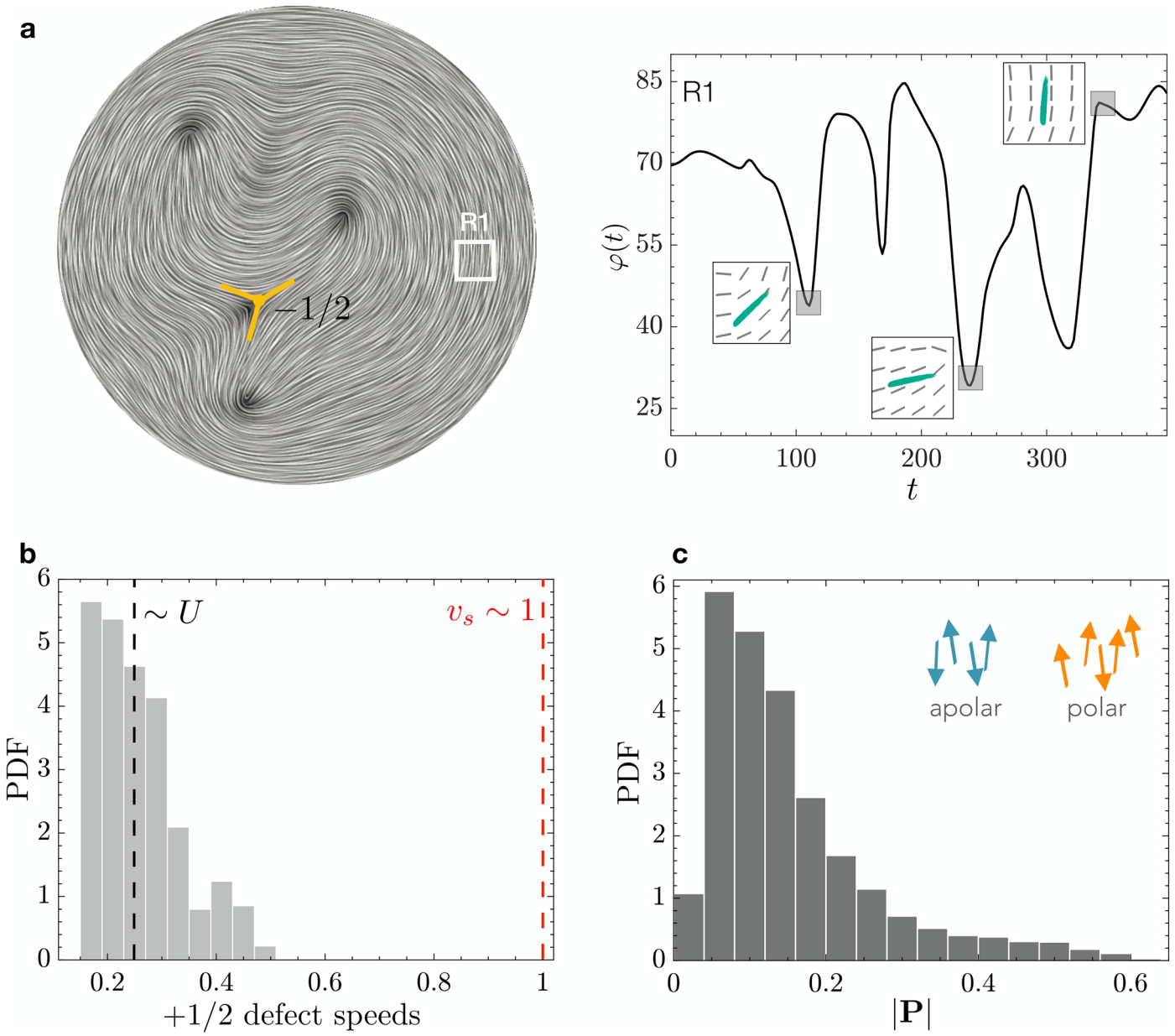

Extended Data Fig. 7 | Director orientation dynamics and statistics of the material velocity *U* and polarity *P* from continuum simulations. a, *Left*: Snapshot of the director field of the flagellar material from simulations of the hydrodynamic model in a disk, displayed using Line Integral Convolution (LIC), where the color encodes the strength of the nematic order parameter *S*. A -1/2-order defect is highlighted in yellow. *Right:* Plot of the evolution of the local director orientation in R1 (white box); insets show the spatial director organization. We estimate a dimensionless time scale $\tau \sim 30$ for the organization of the material and an associated velocity scale $U \sim R/\tau \sim U_{\text{defects}} \sim 0.3$, where *R* is the system size. **b**, Histogram of the distribution of the defect speeds U_{defects}, estimated by tracking +1/2-order defects. For the chosen parameters (Supplementary Section IV.G), the swimming speed of flagellar segments $v_s \sim 1$ is separated in scale from the average material speed, as observed in experiments (Fig. 2g in the main text, Supplementary Video 3). This direct measurement of defect speed is in agreement with the scaling estimate obtained using the material vorticity. **c**, Histogram of |**P**| sampled across the simulation domain, demonstrating the largely apolar nature of the material. Schematized arrows reflect the microstructural organization of sperm segments in qualitatively different regions of |**P**|.

https://doi.org/10.1038/s41567-026-03305-4

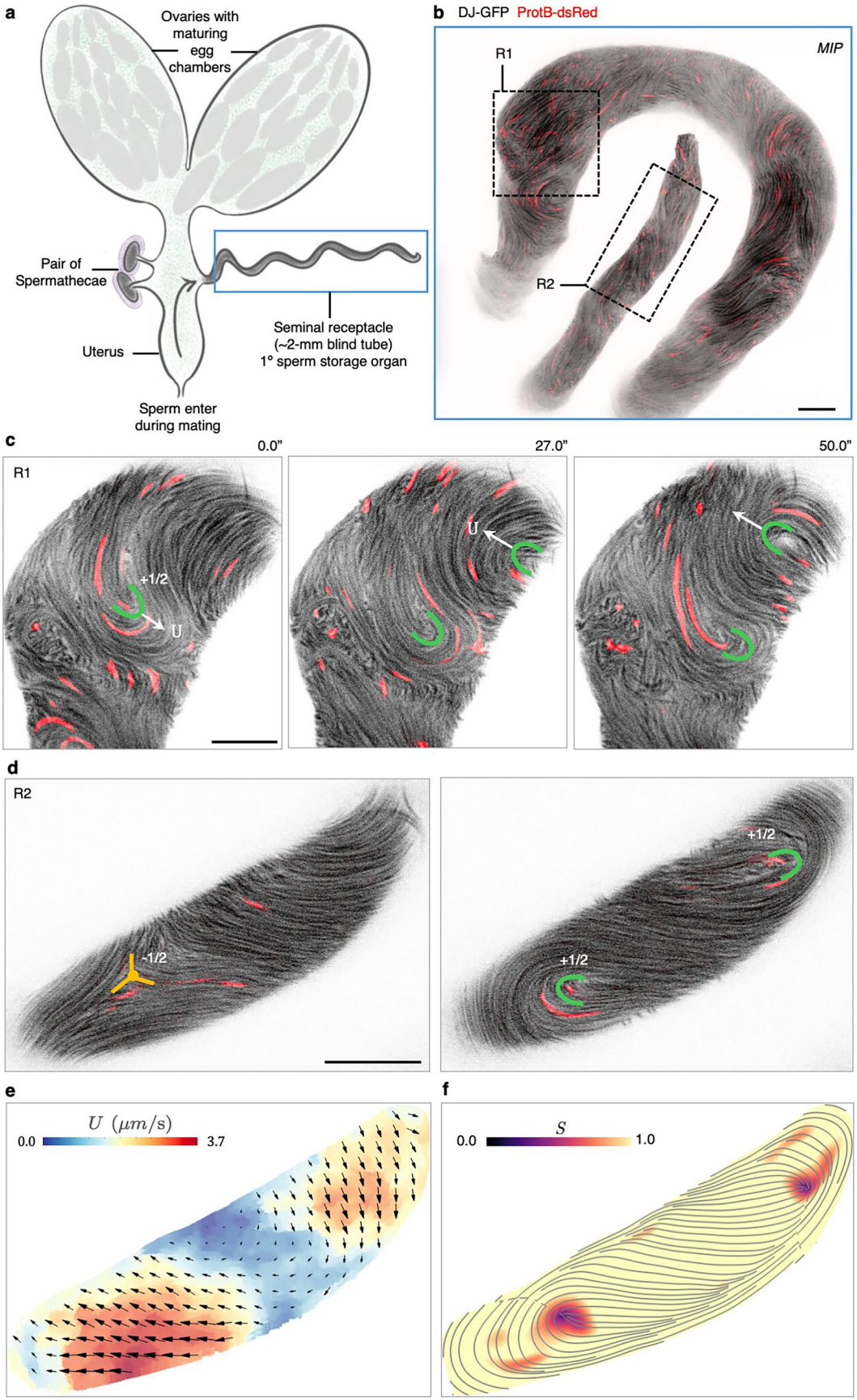

Extended Data Fig. 8 | See next page for caption.

https://doi.org/10.1038/s41567-026-03305-4

Extended Data Fig. 8 | Qualitatively similar sperm organization and dynamics in the female's seminal receptacle (SR) as in the male's SV. a, Simplified schematic of the *Drosophila melanogaster* female reproductive system. A pair of ovaries houses developing egg chambers, which give rise to the oocyte (egg cell). During mating, sperm deposited in the uterus navigate to the sperm storage organs (SSO), where they remain until fertilization for up to two weeks. The primary SSO is a blind ~ 2-mm tube called the seminal (or ventral) receptacle (boxed), where most (~ 80%) of the sperm are stored[25]; the rest are stored in a pair of mushroom-shaped organs called the spermathecae. **b**, MIP (~ 40μm deep) of stored sperm with fluorescently labeled heads (ProtB-DsRed) and flagella (DJ-GFP) in the seminal receptacle. Snapshots of optical sections from time-lapses of the boxed regions are shown in **c** (R1) and **d** (R2). **d**, Snapshots from a time-lapse highlighting a pair of +1/2-order defects moving in opposing directions with speed U in the wider (posterior) region of the seminal receptacle (diameter ~ 30μm). **e**, Snapshots from a time-lapse showing the emergence of +1/2- and −1/2-order defects in the narrower (anterior) region (diameter ~ 10μm) of the seminal receptacle. As in the male's SV, sperm's flagella in the female's seminal receptacle are highly aligned, resembling a continuous nematic material with spontaneously emerging and slowly moving defects. Individual sperm, in contrast, counter-propagate within lanes formed by the flagellar backbone. Scale bars in **b**-**d** = 10 μm. **e**, Material velocity field, with the magnitude of U color-coded; arrows are velocity vectors. **f**, Nematic order-parameter and the associated director field, indicating that sperm in SR are highly aligned (S ~ 1) with loss of order close to defects. Through measurements of the relative motion of contiguous head pairs in the SR, using the same separation distance criterion as in the SV (see Fig. 3b), we also found that in 75% of cases, sperm propagate in opposite directions (n = 175 pairs from 3 SRs), and do so relatively quickly (v_s ~ 28.5 ± 7.8μm/s, n = 14 sperm) compared to the material speed (U ~ 5.5 ± 2.6μm/s, n = 15 + 1/2 defects).